UNIVERSITAT POLITÈCNICA DE CATALUNYA
BARCELONATECH
Escola d'Enginyeria de Telecomunicació
i Aeroespacial de Castelldefels

DEGREE FINAL PROJECT

TFG TITLE: Design, simulation and testing of a downforce-increasing car bodykit

DEGREE: Air Navigation Engineering Degree

AUTHOR: Marc Maceira Gallego

ADVISOR: José Ignacio Rojas Gregorio

DATE: 8th of February, 2019

Títol: Disseny, simulació i testeig d'un kit de carrosseria aerodinàmic per a turisme

Autor: Marc Maceira Gallego

Director: José Ignacio rojas Gregorio

Data: 8 de Febrer de 2019

Resum

El present projecte tracta sobre el disseny i anàlisi del comportament d'un vehicle amb apèndixs aerodinàmics afegits sobre la geometria de fàbrica en túnel de vent virtual. El modelat dels mateixos s'ha dut a terme amb l'objectiu d'augmentar al màxim la força de sustentació negativa, comprometent el mínim possible la resistència aerodinàmica. Per a tal, s'han emprat els programes SolidWorks, per a generar el model CAD (Disseny Assistit per Ordinador) base i la geometria addicional, i el codi obert OpenFOAM, per a dur a terme les simulacions CFD (Dinàmica de Fluids Computacional) i extreure'n els resultats.

Una primera aproximació ha estat duta a terme emprant el model genèric àmpliament estudiat conegut com a Ahmed Body, simulant un cas incompressible i estacionari amb flux turbulent; s'ha usat el solver simpleFoam i el model de turbulència K-omega SST. S'ha assolit una correcta similitud amb dades experimentals publicades i s'han validat ambdós model inicial i malla.

Posteriorment, s'han desenvolupat models de 3 alerons, 3 spoilers, 3 altures, 3 difusors, 2 splitters frontals, 2 làmines laterals o "side skirts" i 2 canards. La contribució de cadascun dels elements en les forces experimentades pel cos estàndard (lift i drag) s'han estudiat per separat. El component que ha mostrat una contribució major a la generació de sustentació negativa ha estat l'aleró NACA 6412 a 15º d'angle d'atac (AoA). Finalment, s'ha simulat un primer model (final AB1) incorporant els elements que han suposat una major contribució a la generació de sustentació negativa. L'eficiència aerodinàmica del model inicial era de E = 0.795. Amb el model final AB1 s'ha assolit E = -1.519. Dues altres configuracions han estat estudiades per a verificar si s'havia assolit el màxim global de sustentació negativa: els resultats indiquen que el model final AB1 suposa la màxima força de sustentació negativa, mentre que el model final AB3 suposa la major reducció en resistència aerodinàmica.

Un segon anàlisi ha estat dut a terme sobre un model simplificat d'Audi R8 V10 2017, per a comparar els efectes de la geometria desenvolupada sobre un model de cotxe més proper a la realitat. Sobre el model final s'han estudiat el canvi en velocitat de pas per curva i el consum. La velocitat de pas per curva ha augmentat en un 1.57%, mentre que el consum ha pujat un 4.73%, respecte el model inicial d'Audi R8.

Title: Design, simulation and testing of a downforce-increasing car bodykit

Author: Marc Maceira Gallego

Advisor: José Ignacio Rojas Gregorio

Date: 8th of February, 2019

Overview

The following project depicts the design of a car body kit and its consequent aerodynamic analysis on virtual wind tunnel using Computational Fluid Dynamics (CFD) software. The aim is to increase downforce as much as possible while keeping drag at a decent value. SolidWorks has been used to create the initial Computer Aided Design (CAD) model of the car and the aerodynamic appendices, and OpenFOAM open source code serves as the CFD simulation and analysis platform.

A first simulation has been carried over standard Ahmed Body, an extensively investigated geometry. An incompressible, turbulent, steady-state case has been assumed: simpleFoam and K-Omega SST have been chosen as solver and turbulence model respectively. Good agreement with published data has been achieved regarding the initial model's behaviour, and the mesh and initial model have thus been validated.

Later on, the external components to be tested have been developed: 3 spoilers, 3 wings, 3 diffusers, 3 ride heights, 3 front splitters, 2 side skirts and 2 canards. The contribution of each of the components to downforce and drag has been studied individually. The component that contributes most effectively to increasing downforce is the 15º Angle of Attack (AoA) NACA 6412 rear wing. A first final car model has been developed using each of the components in the configuration that demonstrated a higher contribution to downforce generation. The initial model's efficiency was found to be E = 0.795. With the corresponding modifications, the final model 1 had an efficiency of E = -1.519. Two other models with different configurations of the components were tested to confirm whether we achieved the global optimum or not, and the results indicate that final model AB1 achieved the maximum downforce, while final model AB3 achieved the lowest aerodynamic resistance.

A second analysis performed over a 2017 Audi R8 V10 simplified model has been carried as well, to observe the effects of the developed appendices over a more realistic car shape. Turn velocity and consumption have been studied over the final R8 model. The turn velocity has increased in 1.57%, while the consumption has increased in 4.73%, with respect to the standard R8 model.

To dad, from whom I inherited the passion for drawing and imagining new things.
To mom, for teaching me on being tenacious and patient.

GENERAL INDEX

INTRODUCTION

In the early days of automotive industry, automobiles were built with a single purpose: transporting people or goods. If we look at cars like the 1908 Ford T, for example, it becomes clear that they were not very aerodynamic or streamlined back then. But years passed by, and manufacturers started focusing more and more on not only forcing the car to move by means of its engine, but also using the air around it to obtain certain advantages.

The objective of this project is to try to understand the effect that certain aerodynamic appendices have on the behaviour of a car. To do so, we will first design our models in SolidWorks, a 3D Computer-Aided Design (CAD) software which is really helpful for creating the desired geometries, and in which we already have some experience thanks to the lectures imparted during the second grade of College. Once the models are done, we will use OpenFOAM, an open-source C++ library of applications for Computational Fluid Dynamics (CFD), where we will introduce our model and perform simulations in order to obtain certain results.

We will try to decompose the work in several sections:

- First, we will design the overall shape of the body in SolidWorks. The objective is to analyse the flow around a 2017 Audi R8 V10, but since there is not much data available on the aerodynamic behaviour of this car, we will make use of the baseline reference Ahmed Body to create and refine the mesh, develop the appendices and assess their behaviour and effect. Further detail regarding Ahmed Body is provided in chapter 2.

- We will generate a mesh around our body, define the initial and boundary conditions and perform a first simulation to observe the behaviour of our initial model. More specifically, we will focus on drag coefficient as our reference parameter. Once the initial mesh is created, we will perform a mesh independence study, refining the latter and varying its dimensions until we achieve convergence on the results.

- Then, we will try to enhance certain characteristics of the concept by changing its geometry and simulating again with the same conditions used in the first attempt. This way, we will be able to compare the results obtained with and without the bodykit “installed” on the car. The main focus of the analysis will be put on drag and lift forces acting over the car, so the goal is

to increment downforce as much as possible and see if the drag tradeoff is worth it.

The resources used for this project have been the following:

Workstation:

- AMD Ryzen 7 1700 @ 3.0 GHz, 8 core processor
- GSkill Ripjaws V, 16GB single RAM module
- Asus x Radeon RX550 series, 4GB graphic card
- Samsung 860 EVO 500GB SSD

Software:

- OpenFOAM 6.0
- ParaView 5.8
- SolidWorks 2018
- OnShape
- MatLab R2018b

CHAPTER 1. Theoretical background

1.1 - Fundamental equations governing fluid dynamics

Fluid dynamics is a discipline that lies in the field of physics. It focuses on studying the forces that act upon a moving fluid, be it liquid or gas, and how it interacts with its surroundings (for example, submerged bodies). CFD does just that, but relying on virtually recreated environments.

Fluid dynamics can be described by means of the flow governing equations, which in fact represent the conservation laws of classical physics.

1.1.1 - Mass conservation equation

The continuity equation states that the rate at which mass enters a system equals the rate at which mass leaves a system plus the accumulation of mass within that same system (eq. 1.1).

$$\frac{\partial \rho}{\partial t} + \nabla(\rho \cdot \mathbf{U}) = 0$$

The time derivative term accounts for the accumulation, or loss, of mass in the system, while the divergence stands for the difference between flow in and flow out. If we consider an incompressible fluid (density = ct.), and no changes in time (steady problem) (eq. 1.2):

$$\frac{D\rho}{Dt} = 0$$

the mass continuity equation can be simplified into a volume continuity equation (eq. 1.3)

$$\nabla \cdot \boldsymbol{U} = 0$$

which means that the divergence of the velocity field is zero everywhere, or that the local volume dilation rate is zero.

1.1.2 - Momentum conservation equation (Newton's 2nd law)

The momentum conservation principle states that the rate of momentum change over a fluid particle can be expressed as the sum of all the forces acting over said particle (eq. 1.4).

$$\rho \frac{D\boldsymbol{U}}{Dt} = -\nabla P + \rho \boldsymbol{g} + \mu \nabla^2 \boldsymbol{U} + \frac{1}{3}\mu(\nabla \cdot \boldsymbol{U})$$

Also known as the Cauchy equation, note that the viscous stress tensor has been expanded as in the Navier-Stokes convective form, accountable for any kind of fluid.

Assuming incompressibility again, and negligible gravitational effects (eq. 1.5):

$$\frac{\partial \boldsymbol{U}}{\partial t} + \boldsymbol{U} \cdot \nabla \boldsymbol{U} = \frac{-\nabla P}{\rho} + \nu \nabla^2 \boldsymbol{U}$$

1.1.3 - Energy conservation equation

The energy of a fluid is commonly considered as the sum of the internal or thermal energy , the kinetic energy and the potential or gravitational energy. Hence, the rate of change of energy in a fluid particle is the sum of the net heat change and the work applied to said particle (eq. 1.6)

$$\frac{\rho DE}{Dt} = -\nabla \cdot (P \cdot \boldsymbol{U}) + \left[\frac{\partial \boldsymbol{U}\tau}{\partial x} + \frac{\partial \boldsymbol{U}\tau}{\partial y} + \frac{\partial \boldsymbol{U}\tau}{\partial z}\right] + \nabla \cdot \big(k\nabla(T)\big) + S_E$$

1 2 3

1. The first term represents the work done by forces -normal and tangential- to the surface, respectively.

2. The second term is the diffusive term, which accounts for energy transmission by convection or conduction.

3. The third term comprises external energy sources, like solar or electromagnetic.

The hypotheses for the fluid defines it as a Newtonian and incompressible fluid. Hence, the energy equation can be solved separately: it is de-coupled. We will also consider our fluid as a continuum, which means that only macroscopic effect will be taken into account (for fluid particle, let us define an infinitesimal fluid volume of volume *dV*). In addition, since the solver used will be a steady-state one, the time-derivative terms are reduced to 0.

1.2 - Lift generation

When a certain object makes contact with a fluid that moves at a relative speed with respect to said object, some peculiar behaviours can be observed. One particularly interesting phenomenon is the generation of fluid dynamic forces.

A fluid volume can be decomposed in several volume differentials, each of which has its own pressure value. When an object enters the fluid volume at a certain speed, it exerts a force over the fluid in front of it, pushing it out of the way and creating a certain pressure distribution on the fluid volume. If the pressure is different at different points, then integrating the overall pressure will give us a net value, either positive or negative, or zero. That pressure, multiplied by an area, equals in a force. Said force usually has two components: lift (perpendicular to the incident direction of the flow) and drag (parallel to the incident direction of the flow). Drag is always present, but lift depends highly on the obstacle's shape and position with respect to the flow. For example, a symmetrical wing (like NACA 0012) does not produce any lift at an angle of attack (AoA) of 0º, but it does for either positive or negative AoA.

Let us look at a flat plate, for instance. If the plate is parallel to the flow, it will only experience a slight drag due to the frontal area facing the flow, but it will not produce lift. Now, if we tilt the plate in a clockwise manner around the leading edge, then air is deflected downwards. This deflection in the direction of air is a result of a force being applied by the plate to the air. Hence, in consonance with Newton's third law, the air applies an equal force of opposite direction on the plate, which is pushed upwards.

Nevertheless, the air that goes above the plate quickly detaches due to a sharp change in the geometry. That is why airfoils are shaped like water droplets, to avoid flow detachment over the top. This happens thanks to the Coanda effect. The key, though, is the fact that the leading edge has to be higher with respect to the trailing edge, so that the net flow of deviated air has a downward component. Or, in the case of car wings, an upward component: hence why car wings are like aircraft airfoils, but put upside down.

1.3. Venturi tunnel

The Venturi tunnel principle can be applied to cars in order to avoid positive lift generation. The idea consists on creating a narrow channel underneath the car for air to flow through. The Venturi tunnel works based on the assumption of incompressible flow, which is made here (Mach (M) < 0.3). It states that, for a flowing fluid, when it sees its cross-sectional area reduced, its speed must increase in order to comply with energy and mass conservation, and thus its pressure must decrease. If pressure decreases underneath the car and becomes lower that the pressure above it, then negative lift (also known as downforce) can be achieved.

All in all, when we analyse the behaviour of a car with respect to the air in its surroundings, we find two main forces that act on its surface when moving:

- Drag, which pushes the car backwards (that is, in opposition to its forward motion).
- Lift, that can be either positive (lifting the car upwards) or negative (pushing the car to the ground).

The main objective of car aerodynamics is to take as much advantage as possible from those forces. Such thing can be done from two basic perspectives:

- Increase the performance of the vehicle (maximize the speed and the grip in straight legs and/or in turns).
- Reduce its fuel consumption by reducing drag.

In our case, we will focus on improving the performance of the car; thus, its overall downforce must be increased without generating excessive drag. With that, traction will be improved, and the power will be transmitted to the road with less losses, achieving the same effect as if we increased the weight load on the car; but actually, we are just adding the weight of the aerodynamic components, which can be fabricated in, for example, carbon fiber reinforced epoxy; making them extremely light and resistant.

Moreover, with a good CFD or wind tunnel analysis, high-pressure areas over the surface of the car can be identified. Air intakes can then be placed in such areas to guarantee an optimal cooling of the engine, the brakes, etc. However, accounting for the internal flow of air through a vehicle requires higher computational power and resources, so that is left out of the scope of this project.

CHAPTER 2. Initial model

When choosing which guidelines to follow for the initial design, we wanted to recreate a street legal car, in order to make the CFD simulation more realistic. But extensive analytical data is often difficult to find for such models, so instead we decided to first investigate the behaviour of a well renowned model as is the Ahmed Body, test the appendices on this reference geometry and then try to implement the developed appendices to a real car model.

The Ahmed Body has been a commonly investigated geometry in the field of car aerodynamics, so reliable papers about it can be easily found. The initial Ahmed Body model was extruded in SolidWorks following the original blueprints from Ahmed et al. [1]. The chosen angle for the rear slant was 25º, to enable comparison with the results obtained by Petteri [2].

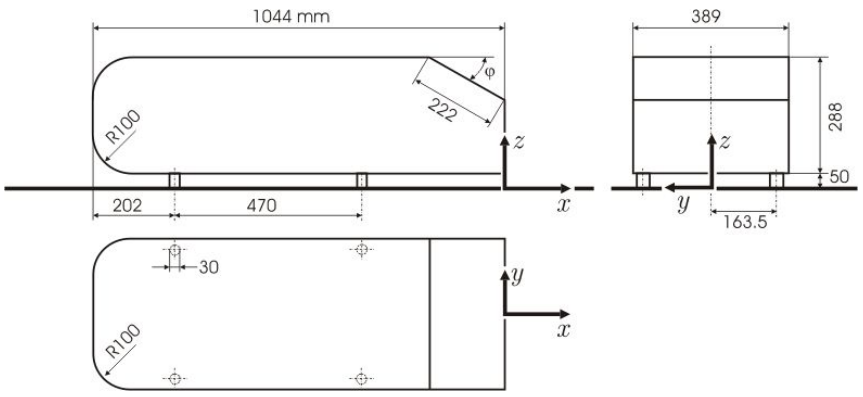

Figure 2.1: Blueprints of the Ahmed Body and reference frame used in this work [1]

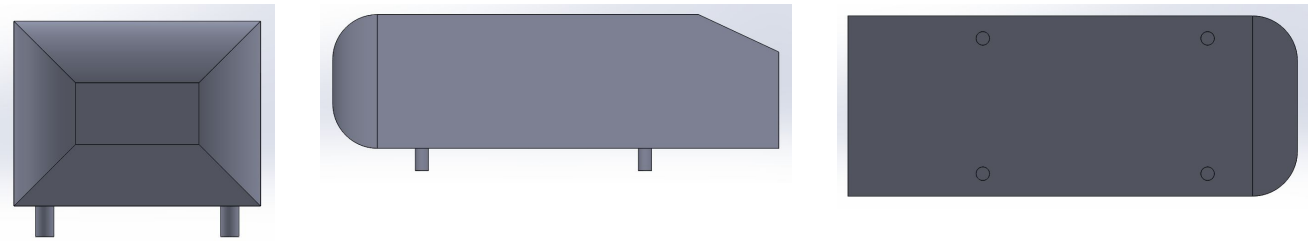

Figure 2.2: Ahmed Body model created in SolidWorks

Once the components have been simulated on the Ahmed Body, they will be exported to a 2017 Audi R8 V10 model and adapted to the dimensions of the latter. For the R8, the real dimensions have been used in a similar manner as with the Ahmed Body, using the official blueprints for its extrusion [3].

When performing a CFD simulation over a certain geometry, one has to take into account that the more complex the model is, the more difficult the generation of the mesh around it will be; as a result, the time and computational resources needed for the meshing and also the simulations will be larger. In regard of that, instead of taking an existing CAD model of the R8, which would have had so many aerodynamically irrelevant details, difficulting the CFD analysis, we decided to recreate its overall shape in SolidWorks while omitting some specific features like the mirrors, front grill, air intakes, number plate holders, windshield wipers, etc. That has been done by extruding a rectangular prism and overlapping the blueprints over its three main planes: top, front and right.

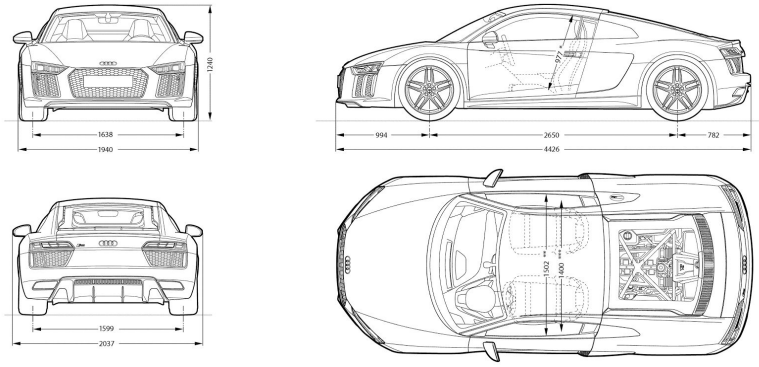

Figure 2.3: Blueprints of the 2017 Audi R8 V10 [3]

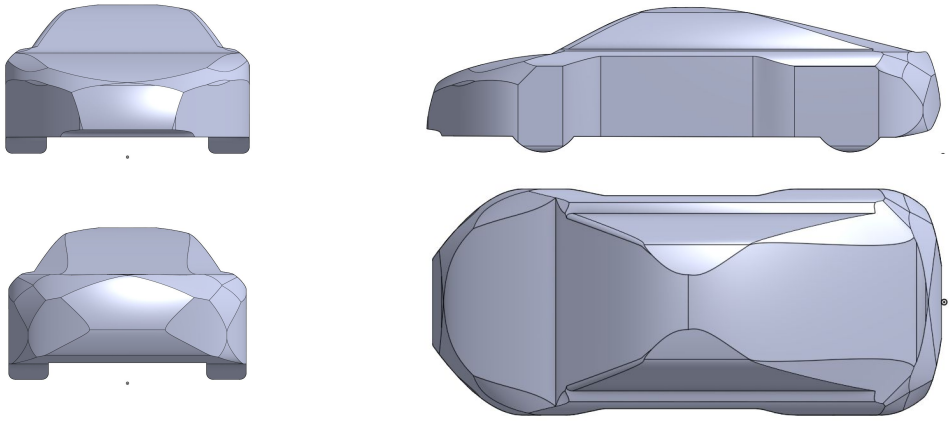

Figure 2.4: Finished CAD model for 2017 Audi R8 V10

CHAPTER 3. Pre-processing

For all the processes involved in CFD simulation, we have used OpenFOAM v6.0 [4]. OpenFOAM is an open-source CFD tool developed in the Imperial College of London, London (UK), and officially launched in 2004. It consists of several C++ modules that allow for analysis and resolution of a wide range of fluid-flow problems, from those involving chemical reactions, such as combustion, to turbulence modelling for aerodynamics.

OpenFOAM's major strength resides in its open-source architecture. Unlike commercial CFD packages, which resemble a black box where the user inputs some conditions and then gets data out, OpenFOAM allows the user to read all the dictionaries containing the functions of the code, making it easier to understand the underlying processes that are carried in the simulation. Moreover, given a specific problem, the user can modify certain modules of the software and adapt them to his/her particular case. This makes OpenFOAM a very versatile software. We decided to install OpenFOAM in an Ubuntu virtual machine (VM), since its performance is best in said operative system.

3.1 - Mesh parameters setup

Once the CAD model of the initial geometry has been created, we head to our Ubuntu VM and create a new directory in the desktop. There, we copy the files from *$FOAM_TUTORIALS/incompressible/simpleFoam/motorbike*, a case tutorial for incompressible turbulent flows around 3D bodies using the K-Omega SST turbulence model and *simpleFoam* steady-state solver. The case is composed of the following files, which can be classified into three main categories (see Fig. 3.1.1.):

- 0 folder: contains the scripts for the initialization of the physical values in the different patches that compose our geometry. Each of the ones shown below, out of the include folder, define how the variables should be treated in every specific patch.

    - *k* or turbulent kinetic energy.
    - *omega* or specific turbulent dissipation rate.
    - *nut* or turbulence viscosity.
    - *p* or pressure.
    - *U* or velocity.

    - *Include* folder: contains three scripts:

        - *fixedInlet,* where the patch type of the inlet is defined: in our case, *fixedValue.*
        - *frontBackUpperPatches*, where the patch type of the front, back and upper patches is defined: in our case, *slip.*
        - *initialConditions*, where the initial values of *k*, *omega*, *p* and *U* are defined.

- *constant* folder: contains the scripts *transportProperties* and *turbulenceProperties.* In *transportProperties*, the value of kinematic viscosity *nu* is specified, along with its SI units (m^2/s). In *turbulenceProperties,* the turbulence model is specified; in our case, K-Omega SST.

    - triSurface: contains the Standard Tessellation Language (.STL) file of our geometry. The file should be in meters in order to be properly displayed by *paraFoam*.

- *system* folder: contains various scripts that define the meshing process characteristics and various parameters of the numerical aspect of the simulation.

    - *blockMeshDict*: defines the dimensions of the background mesh.
    - *controlDict*: establishes the solver and time step used, the number of iterations, the write interval, etc. Here, the maximum courant number has been set to 1.
    - *decomposeParDict*: used for the parallel computation, defines the number of cores used and their configuration (hierarchical in our case).
    - *forceCoeffs*: parameters like the streamwise velocity, reference area, reference length and lift and drag axis used for the computation of the force coefficients are defined here.
    - *fvSchemes*: sets the numerical schemes for the terms calculated during the simulation, such as derivatives.
    - *fvSolution*: controls the equation solvers, tolerances and algorithms.
    - *meshQualityDict*: establishes the minFaceWeight, a key mesh quality parameter, in our case set to 0.02.
    - *streamLines*: saves the data points for the post-processing of streamlines.
    - *surfaceFeaturesDict*: the geometry used for the intersection with the background mesh should be specified here.
    - *snappyHexMeshDict*: the main dictionary for the meshing stage.

Figure 3.1.1: motorbike tutorial directory

In order for ParaView to display the model, we have to convert it to .STL file, an extension commonly used in the 3D printing world. It creates an approximation of the real file by replacing its surface with triangular planes, but it does not display features like color or texture. Two .STL representations exist: ASCII and binary. Although binary .STL files are more compact, we found some incompatibilities between binary files and ParaView 6.0.

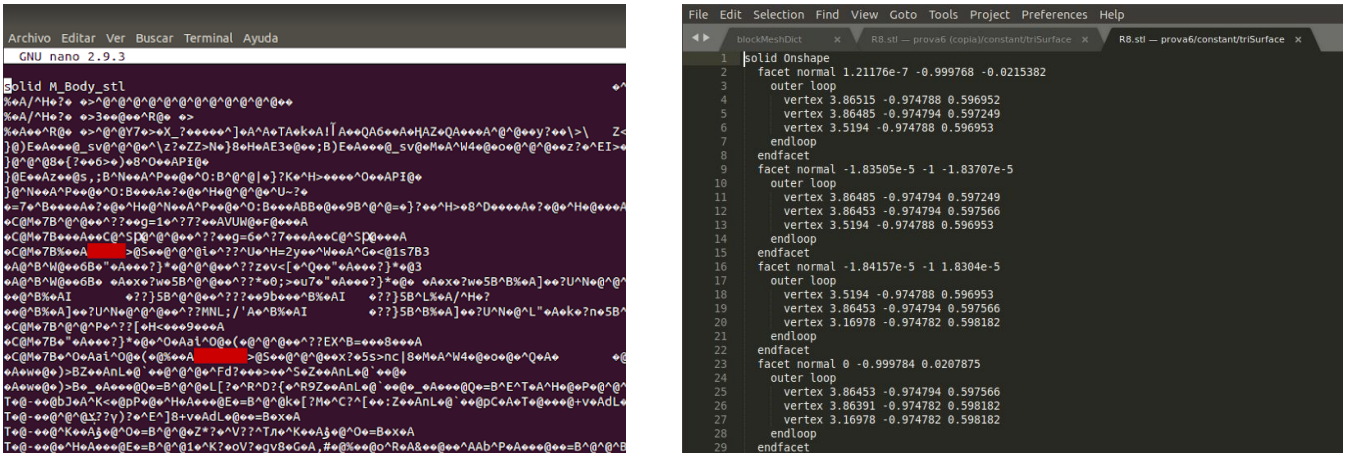

Figure 3.1.2: Binary STL (left) and ASCII STL (right)

When trying to import our CAD geometry into ParaView, the software did not recognise the file's format, so we ended up opening our file in OnShape and saving it as ASCII .STL from there; this way we were able to visualize the CAD file without problems, and also modify the first and last line, which have to coincide with the file name for it to be displayed. To check that we can visualize our .STL file without problems, we can execute a simple order on the terminal of our Ubuntu VM:

paraView

This will open ParaView, and from there we can just load our .STL file and click Apply.

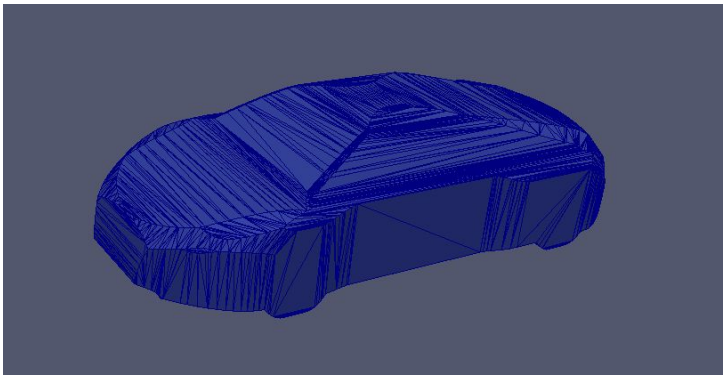

Figure 3.1.3: .STL file loaded in paraView

Given that our project implies developing geometry which will not always sit on the symmetry plane of our model (in this case, the X-Z plane), we have chosen to develop a 3D mesh using *snappyHexMesh.* The process of creating and refining this mesh is a bit more complicated than other methods, but it allows for a more realistic approach to the case, since it accounts for 3D effects.

3.2. snappyHexMesh parameters setup

SnappyHexMesh is an OpenFOAM utility which generates 3D meshes containing hexahedra and split-hexahedra volumes from triangulated surface geometries in .STL or .OBJ formats. It allows for high customisation of several meshing parameters, which makes it very flexible to the user's model and preferences. Its information is contained in *snappyHexMeshDict.*

One requirement for running *SnappyHexMesh* is a previously generated *blockMesh*, which is a background mesh composed solely of hexahedrons. The .STL file is then imported into the same environment where the background or "bounding" mesh is, and must be located inside the domain of said mesh.

That can be done by modifying the boundary parameters on *blockMeshDict*. One advantage of paraView is that it can run in parallel, allowing us to check our progress step-by-step.

Once the .STL file is located inside the bounding mesh, we can type in:

paraFoam &

into the terminal and a temporary *Foam* file will be created on paraView. We click apply to see the background mesh, and then open our .STL file, located in *constant/triSurface*. From here on, the mesh generation process of *snappyHexMesh* consists of three steps (see Figs. 3.2.1, 3.2.2 and 3.2.3):

- *castellatedMesh:* We give *snappyHexMeshDict* a three-coordinate point, in our case a point located outside of our .STL file, but inside the bounding mesh. This indicates that we want to keep the mesh region outside of our body, since we are performing an external flow analysis. The application then detects the spots where the .STL file's profile intersects with the cells of the background mesh, and deletes the cells that have 50% or more of their volume located inside the .STL file. This leaves us with a mesh that's more or less rough, depending on the level of cell refinement specified near the edge of the .STL (see Fig. 3.4):

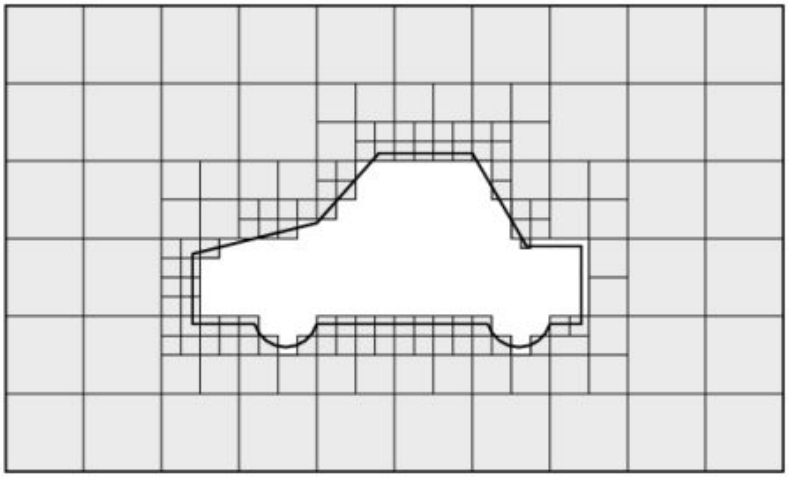

Figure 3.2.1: Cell removal in snappyHexMesh meshing process

- *snap:* Now, the vertices of the cells located inside the .STL's volume are brought back to be aligned with the surface of the .STL. The application then checks for vertices that cause mesh quality parameters to be non-compliant, and tries to reduce their displacement iteratively until the target mesh quality

is satisfied. This step is known to have problems with very aggressive geometries, so we have tried to create an initial model that is as smooth as possible.

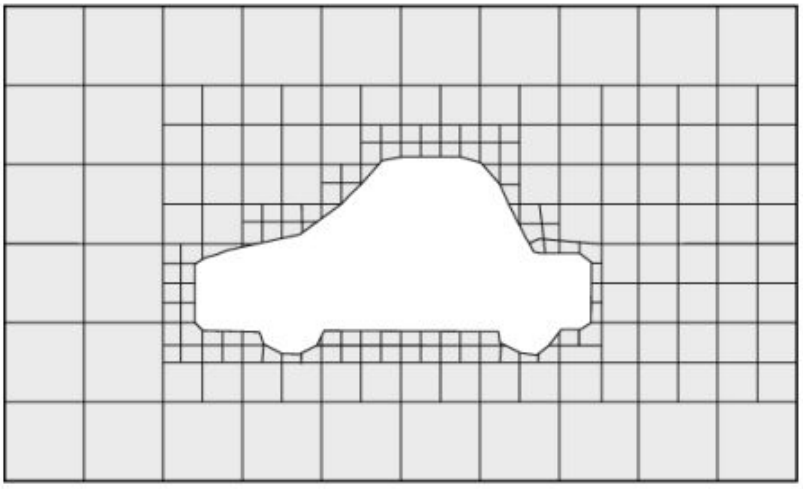

Figure 3.2.2: Surface snapping in snappyHexMesh meshing process

- *addLayers:* Finally, in order to obtain better precision and resolution near the surface of the object, where the boundary layer (BL) is located, the application adds several layers of mesh near the .STL's profile. This is done by contracting the initial snapped mesh and adding the number of user specified layers, whose thickness can also be specified.

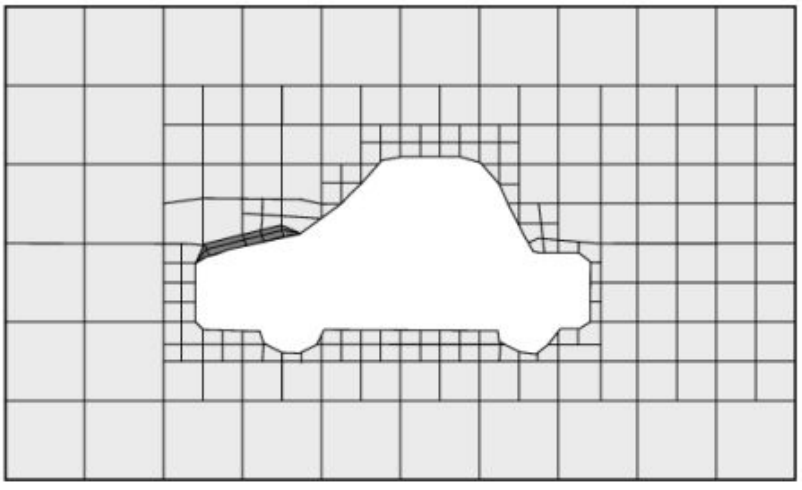

Figure 3.2.3: Layer addition in snappyHexMesh meshing process

3.3. Mesh convergence

In order to attain a minimum of quality in our results, it is of paramount importance to use a proper mesh. This is done by performing a study on mesh convergence, which consists on reading a certain parameter from our analysis, and then successively modifying our mesh until the result obtained is no longer affected by the mesh size. This is commonly called ‘mesh-independent result’.

While the above is the correct procedure to follow, sometimes achieving total mesh-independent results implies enormous amounts of computational resources, which can make the simulation unfeasible. In such case, one should take as valid the finest mesh that can give acceptable convergence in the results. There are two main aspects of the mesh in which we can work to make it more suitable for the simulation: overall size and local refinement.

3.3.1. Size of the mesh

If the mesh is not big enough for our model, the flow could be disturbed and affected by the nearby walls, and also the wake generated behind the vehicle would not be properly computed. For this matter, if we assume the reference length of our model to be L, it is recommended:

- To leave a distance of 3L in front (upwind) of the model, to give room for a good characterisation of the velocity and pressure gradients in said area.

- To leave, at least, 5L meters of mesh behind the model, for accurate resolution of the wake.

The bottom area of the mesh should be tangent to the pillars or wheels. Regarding the top, one should leave enough room to characterise a possible flow detachment over the roof of the car and onto the rear spoiler. Also, the blocking coefficient, defined as the ratio of model-to-total frontal area, should be less than 10%, while the wingspan (or width) of the model should be less than 80% of the width of the control volume [5].

3.3.2. Refinement of the mesh

The level of refinement that should be applied to the mesh in its closest region to the wall of our model depends, basically, on our Re number and the size of the smallest details of the CAD geometry:

- If we are working with low Re values, the viscous term will have a more dominant effect on our flow [6], so we should resolve the entire domain of the BL, down to the viscous sublayer, in order to accurately predict the flow behaviour: this requires a substantially high number of cells close to the wall surface, which in turn increases the computational resources needed.

- As Re increases, the boundary layer's thickness decreases, and our flow is dominated by inertial effects, to the point where we can neglect the contribution of the viscous term [6]. As stated by Ferziger and Perić (2002), "At a high Reynolds number, the viscous sublayer of a boundary layer is so thin that it is difficult to use enough grid points to resolve it". This allows for the implementation of wall functions, which model the turbulence near the wall, letting us decrease the number of cells required.

Wall functions rely on the universal law of the wall, which states that the velocity distribution very close to a wall is similar for almost all turbulent flows. Here is where the y^+ value comes in handy, as it is one of the most prominent parameters when judging the applicability of wall functions to a certain flow.

3.4. Dimensionless wall distance y^+

y^+ gives us a reference of the relative contribution of viscous and inertial (turbulent) effects, depending on its value. It is denoted by [7]. (eq. 3.4.1):

$$y^+ = \frac{y \cdot u_\tau}{\upsilon}$$

where:

- y is the absolute distance from the wall.
- u_τ is the friction velocity
- υ is the kinematic viscosity (μ/ρ)

Figure 3.4.1 depicts the balance of viscous and turbulent contributions.

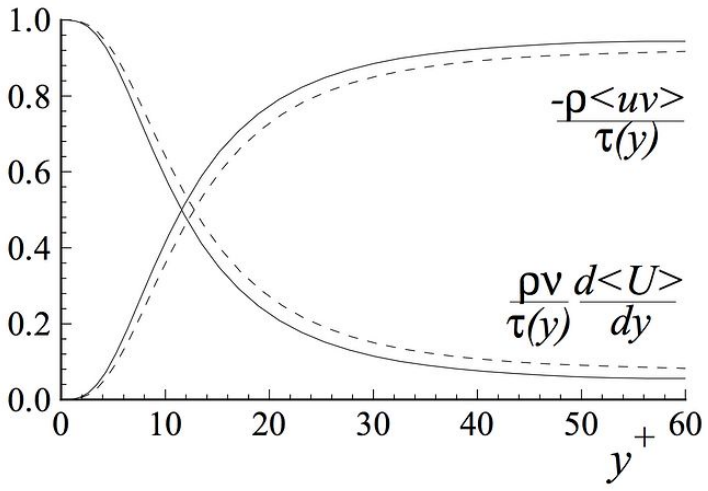

Figure 3.4.1: Profiles of fractional contributions of the viscous and Reynolds stresses to the total stress. DNS (Direct Numerical Simulation) data of Kim et al. (1987): dashed lines, Re = 5,600; solid lines, Re = 13,750 [7]

As can be seen, for values of $y^+ \approx< 10$, viscous effects tend to dominate, as the first cell's center is located in the viscous sublayer. As y^+ increases, inertial effects start to take place, eventually being the major source of contribution to total stress when we reach the outer region of the BL [7].

This means that depending on the kind of flow we want to simulate, we should pick a certain y^+ value in order to correctly apply wall functions. Roughly speaking, any Re above $\sim$13000 is considered to be a high value, since it is around this number where the transition from laminar to turbulent flow begins for air (Osborne Reynolds, 1890). Since we are performing a simulation with high Re (1.33×10^6), we should pick a y^+ value between 30 and 300, commonly accepted for a good characterisation of turbulent boundary layers when applying wall functions [8].

We pick a y^+ value of 100. From here on, we need to obtain the necessary y value, which will tell us how to set the layer addition parameters in *snappyHexMesh*'s Addlayers.

y tells us the size of the first layer, the one which is closest to the model's surface. To obtain said value, we make use of the following equations:

first, we take the definition of y^+ and rearrange for y (eq. 3.4.2):

$$y^+ = \frac{yu_\tau}{\nu} \rightarrow y = \frac{y^+\nu}{u_\tau}$$

Next, we bring up the definition of *frictional velocity* u_τ (eq. 3.4.3):

$$u_\tau = \sqrt{\frac{\tau_w}{\rho}}$$

Now, the *wall shear stress* τ_ω (eq. 3.4.4):

$$\tau_w = \frac{1}{2} C_f \rho U_\infty^2$$

Finally, we compute the *skin friction coefficient* C_f (for a flat plate) (eq. 3.4.5)

$$C_f = 0.0576 Re_d^{-\frac{1}{5}}$$

Inserting our Re value (1.33×10^6) onto equation 3.4.5 and working our way backwards until equation 3.4.2 we obtain the y value. Now we head to the *addLayers* section of *snappyHexMeshDict.*

addLayers allows us to control a variety of parameters for the mesh near the surface:

- Number of layers
- Expansion ratio for layer cell thickness
- Thickness of the final layer
- Minimum overall layer thickness

The user can select arbitrarily the number of layers and the expansion ratio, depending on the level of smoothness of the transition between layers that one wants to achieve. One thing has to be taken into account, though: the thickness of the final hexahedral layer of *addLayers* should be similar to that of the first

hexahedral layer located outside the *addLayers* region. An abrupt transition from a fine cell to a much coarser cell can give inaccurate results in said region, so it is best to first look at the size of the first hexahedral cell, and from here adapt the expansion ratio and the number of layers to coincide with that [9].

Our calculations gave the results shown in Table 3.1:

Table 3.1 - AddLayers parameters

First layer [m]	Nº layers	Exp. ratio	Final layer [m]	Overall [m]
1.8×10^{-3}	5	1.5	9.1×10^{-3}	2.37×10^{-2}

3.5. Mesh validation

The mesh independence study has been conducted by increasing the number of cells in the mesh and checking the obtained Cd (Drag Coefficient) value until a certain saturation in the results appeared. At $\sim 1 \times 10^{6}$ elements there was almost no change in Cd, so we tried to maintain the cell count between 7.5×10^{5} and 1×10^{6} from here onwards. The densities tested and the Cd values obtained are shown in table 3.2 below.

Table 3.2 - Mesh independence study

Mesh density in number of cells	Drag Coefficient for standard AB
$\sim 3 \times 10^{5}$	0.441
$\sim 7.5 \times 10^{5}$	0.393
$\sim 1 \times 10^{6}$	0.392

The validation of the initial mesh has been performed for the standard Ahmed Body, with the following characteristics:

- Length x Width x Height = 1044 mm x 389 mm x 338 mm (height including 50mm legs)
- Characteristic length = 1044 mm
- Frontal area = 0.112 m^2
- Mesh density: $\sim 1 \times 10^{6}$ cells
- Drag coefficient vs. Re in a span of Re = [6.66×10^{4} - 3.33×10^{6}]

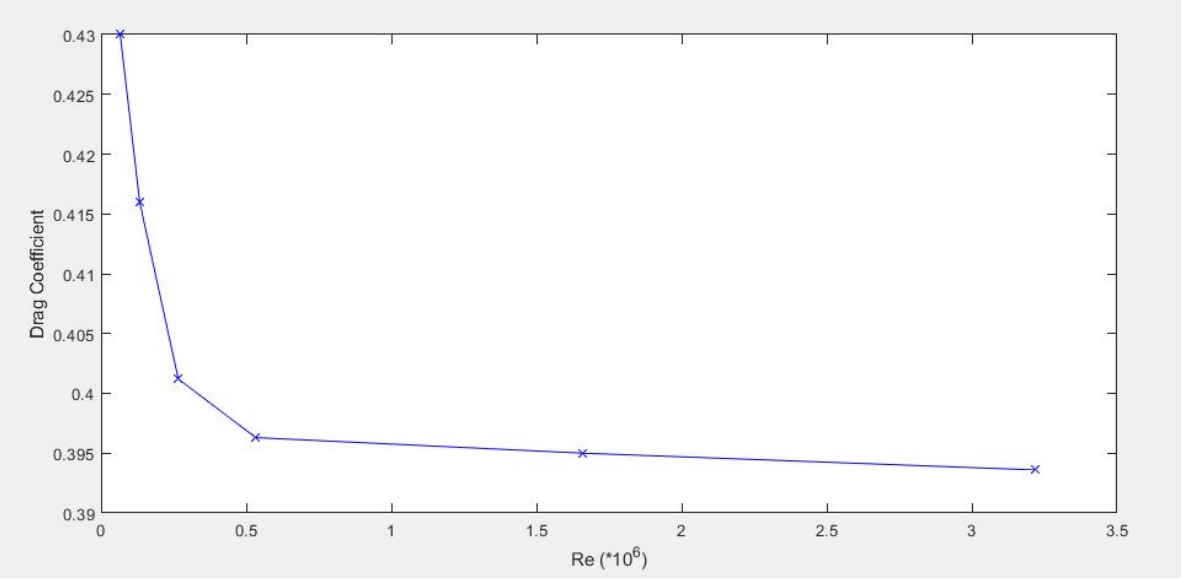

Figure 3.5.1: Drag Coefficient vs. Reynolds number for standard Ahmed Body

The behaviour of the drag coefficient of the standard Ahmed Body is to exponentially decrease as the Reynolds number increases (see Fig. 3.5.1), due to a reduced impact of the skin friction forces. As Re increases, the boundary layer transitions from laminar to turbulent, and it is able to stay attached longer, thus reducing the wake formed behind the body. Such reduced wake implies a reduced pressure drag.

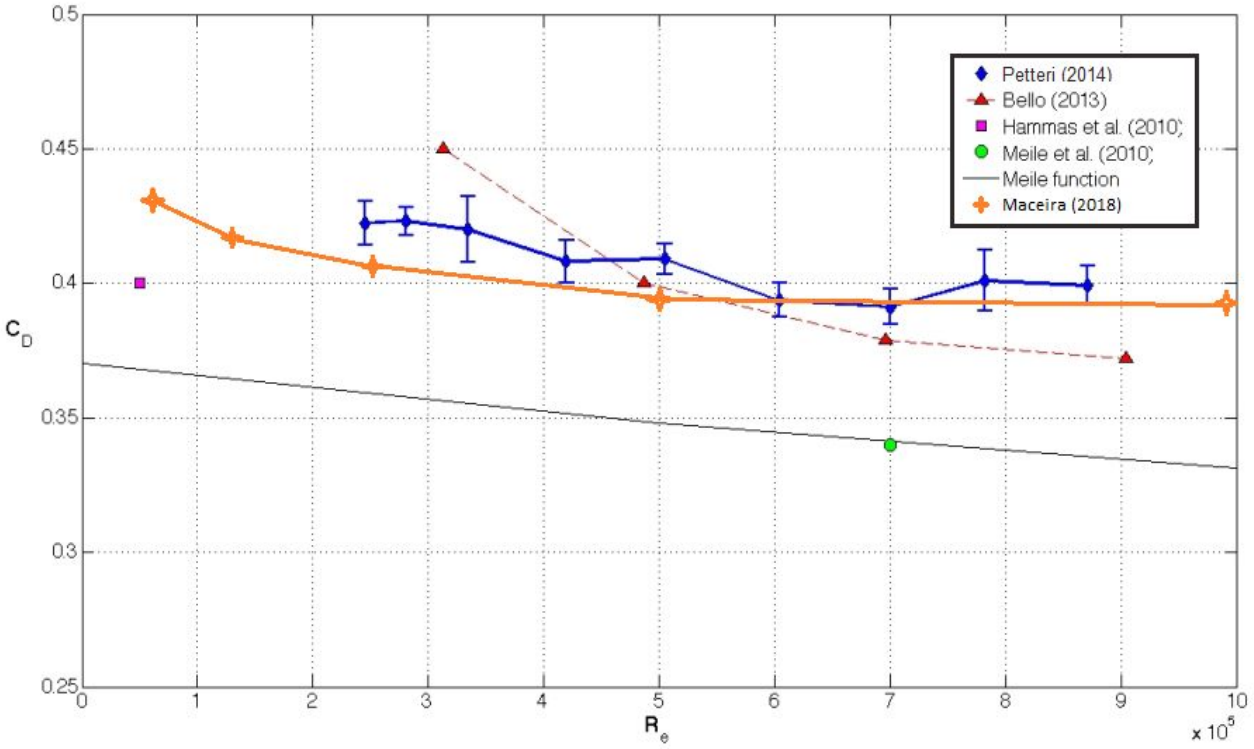

Figure 3.5.2: Cd vs. Re, comparing our results with previous experiments [2]

CHAPTER 4. Solver

4.1. Formulation of the problem

When simulating in a CFD environment for a moving flow, one of the first things to decide is which formulation to use. Depending on the kind of CFD simulation and the level of precision required for the results, one must choose between several options. The two major categories are:

- Laminar: solves the Navier-Stokes equations directly, without having to model the boundary layer region or the turbulent wake. These are good for laminar flows and can be used for turbulent flows also, but in the latter case, this implies using such fine meshes that, for complex geometries, the meshing and calculation times can become unfeasible. One example is direct Navier-Stokes.

- RANS: stands for Reynolds-Averaged Navier Stokes. These models introduce additional simplifying equations that serve the purpose of modeling turbulence, hence allowing for coarser meshes and lower computational costs. Some examples are K-Epsilon, K-Omega, SST.

In our case, we decided to go for a RANS model, precisely K-Omega SST. This model gives a good compromise between K-Epsilon and standard K-Omega. K-Epsilon works best when resolving fields far away from the surface of the body, while K-Omega does the opposite: focuses more on phenomena occurring on the boundary layer. K-Omega SST switches between the two models (K-Epsilon and standard K-Omega) using the aforementioned y^+ coefficient. In reference to [8], it can be used as either a high- or low-Re model, all depending on which y^+ value we choose. Having already stated that our Re is quite high, we chose a convenient y^+ value and meshed consequently.

4.2. simpleFoam solver

The solver used is simpleFoam, a steady-state solver for incompressible, turbulent flow. One must note that, for accurate representation of the vortex shedding which forms behind objects in motion through a turbulent flow, a transient solver is a better option: nonetheless, since the focus of this project is placed on analysing the average forces acting on the body, a steady-state solver allows for lower computational costs, as long as a fairly acceptable convergence is achieved.

SimpleFoam solver uses Semi Implicit Method for Pressure Linked Equations (SIMPLE) algorithm, originally developed by Spalding and Patankar in 1972 [17]. It is an iterative algorithm used for solving Navier-Stokes equations under incompressible, steady-state assumptions. The workflow of this method can be synthesized in the following steps:

- Guess the pressure field, p*.
- Solve the momentum equation to obtain u* and v*.
- Solve the pressure correction equation to obtain p'.
- Calculate p from equation by adding p' and p*.
- Calculate u and v from their starred values using the velocity correction eq.
- Solve all the other discretized transport equations.
- Treat the corrected pressure p as new guessed p*, and return to step 2 until convergence is obtained.

CHAPTER 5: Post-processing and geometry development

Once the validity of the mesh and simulation have been acknowledged through standard Ahmed Body, we proceed to develop the external appendices. The contribution of each one will be analysed individually, in terms of Drag and Lift increase or decrease, and consequently aerodynamic efficiency will be extracted. A flow velocity of U = 20 m/s will be used, in order to maintain a time step equal to 1 second. Note that the tunnel length is 20 meters.

5.1. First model - Standard Ahmed Body

Simulating 1000 iterations for the standard Ahmed Body with a ~1 million hexahedral elements mesh shows good result convergence. The residual values of the three velocity components, pressure, and turbulence parameters k and omega all fall below 0.01%. The oscillations in said parameters' residuals after iteration 300 are due to the formation of a turbulent wake behind the bluff body. Turbulence is unsteady by nature, so a recurrent patron, usually in a sinusoidal form, appears in both residuals and coefficient trackers signifying the existence of a turbulent flow region. The obtained results are shown in table 5.1.

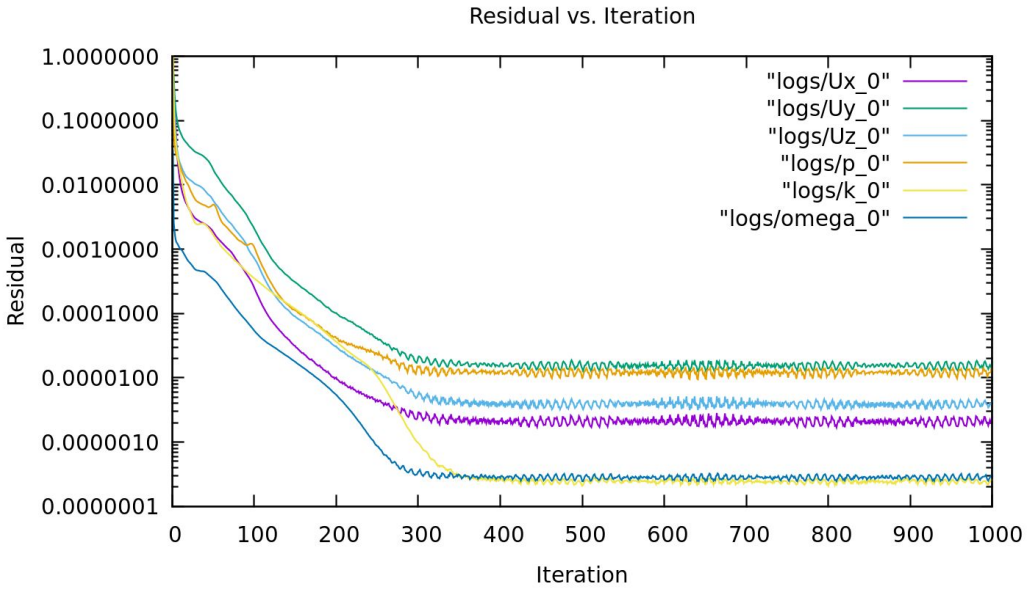

Figure 5.1.1: Residuals of the standard Ahmed Body simulation

Table 5.1 - Forces, force coefficients and efficiency for the standard Ahmed Body

Cl	Cd	Cm	Lift (N)	Drag (N)	Efficiency (L/D)
0.312	0.392	-0.153	9.172	11.524	0.795

5.2. Ride height

When trying to improve a car's downforce, one of the simplest, yet most effective modifications one can do is to modify the suspension (ride height). This directly varies the distance between the bottom of the car and the ground, therefore allowing more or less air to pass below the body. Despite that, a flat undertray and certain ride height must work together with a diffuser in order to achieve the best results possible. In reference to [10], the maximum downforce over a diffuser is achieved by a combination of both a certain diffuser angle and a certain ride height. Different combinations of diffuser angle and heights exist. Standard Ahmed Body sits at 50 mm ride height. Before going any further, we tried to find the optimal ride height so that the diffuser could be as effective as possible.
Table 5.2 (Annex 1) and Fig. 5.2.1 show the main results obtained for four different ride heights, including that of the standard Ahmed Body (AB).

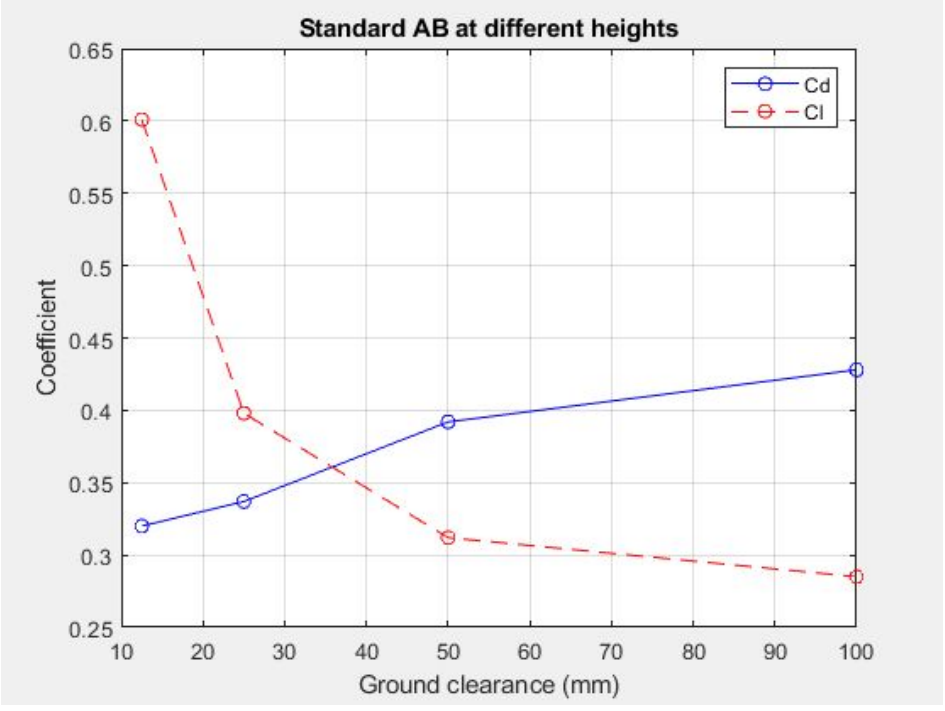

Figure 5.2.1: Force coefficients for standard AB at various ride heights

Ground effect is established when the downwash and wingtip vortices generated by an aircraft's wings or any other vehicle are interrupted by the presence of a near wall, or in this case, the ground. This reduces the amount of induced drag, therefore allowing for higher speeds for a given engine power.

The figure above demonstrates that a simplified bluff body often experiences ground effect in a similar way as a wing does, generating more positive lift the closer to the ground it is. This is due to the influence of viscosity: in reference to [10], inviscid flow would suppose higher downforce for lower ride heights; nevertheless, the viscous effects have a greater impact when the transversal area through which air can flow below the car is reduced.

It can be seen also that the influence of ground effect vanishes as we separate our body from the ground. The critical point depends on the shape and surface of each body. In our case, lift coefficient starts to saturate near 100 mm, so said height will be considered the one to choose for the final model.

5.3. Front splitter

A car acts similarly to that of an airfoil when travelling through air. Some of it goes above the car and some of it goes below. Generally, a low-velocity, high-pressure region can be found in the nose of cars, where air stacks up against the front bumper. If we can prevent that high pressure air from going under the car by separating both zones with a splitter, we can create a pressure difference with respect to the air that flows below, and therefore downforce for the front axle. Fig. 5.3.1 below shows what a typical aftermarket front splitter looks like.

Figure 5.3.1: Aftermarket front splitter on a Honda S2000

The slender profile of the splitter allows it to separate the flow in a smooth manner, and can help direct it to, say, a cooling intake. Aside of that, its main purpose is to increase the effective area in front of the car on which pressure can build up. Table 5.3 (Annex 2) and Fig. 5.3.2 show the main results obtained for three different splitters, with increasing length, compared with the standard AB without splitter.

Figure 5.3.3 shows the advantage of the splitter for splitter number 1: the ability to create a higher pressure zone above and a lower pressure zone below itself. This implies a net positive pressure pressing down on the splitter. Note also how the flow is accelerated earlier, although flow separation exists at the tip of the splitter due to its sharp geometry.

Figure 5.3.4 (Annex 6) allows to visualize how positive lift in the front axle can be greatly reduced by adding a splitter, due to the increased planar area provided. As a counterpart, the general tendency of drag is to increase too, although it does so in a less pronounced way, because frontal area is in fact not increased: the flow encounters the same area when it flows in the X direction (the main velocity axis), because the splitter protrudes alongside the X axis. Therefore, the increase in drag is due to viscous stress over the front plate. Notice how the splitter affects mainly the downforce produced on the front axle (or front half of the body).

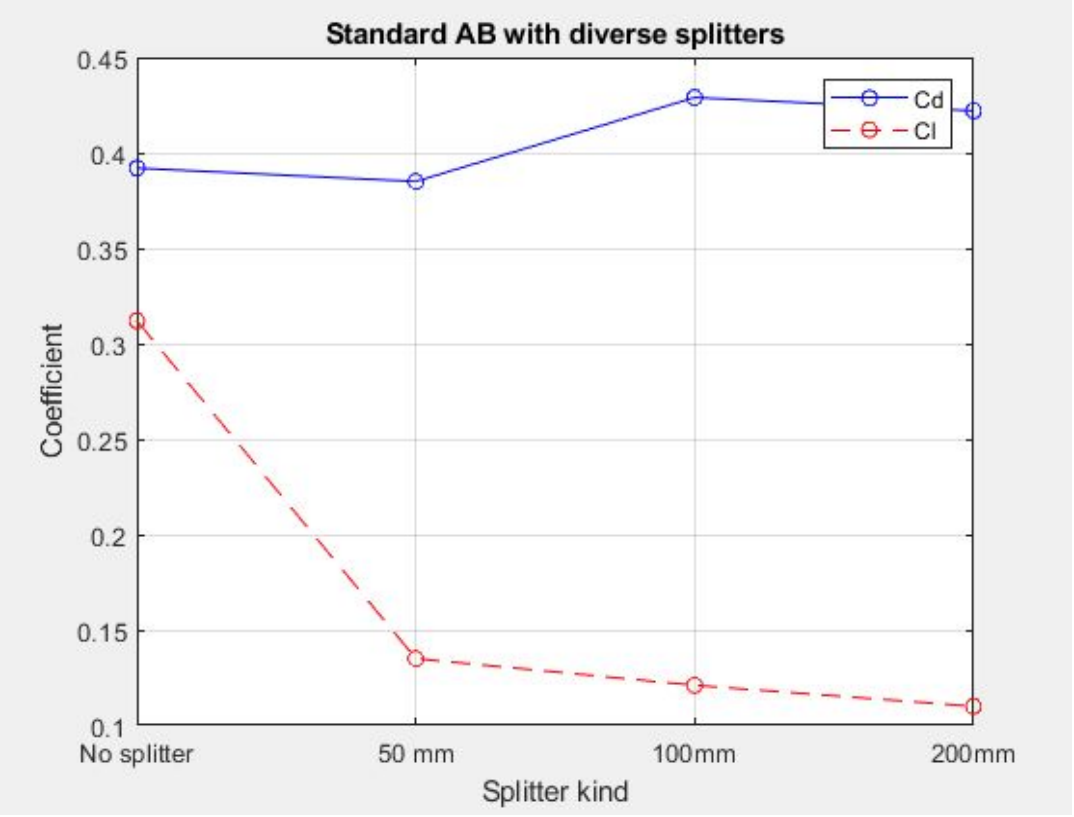

Figure 5.3.2: Force coefficients for standard AB with various splitters

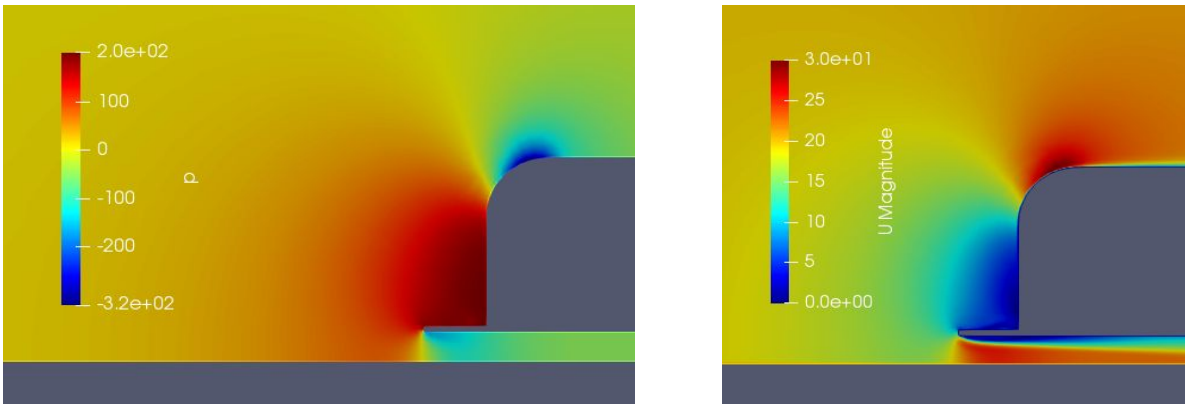

Figure 5.3.3: Plots of contours of pressure relative to steady atmospheric pressure (m^2/s^2, left) and flow velocity contours (m/s, right) for splitter 1

5.4. Side skirts

Following the idea of a splitter, side skirts provide a similar advantage. They are usually placed in the edges of the bottom of the car, and they act as a physical barrier between the upper and lower halves of the body. The air passing above has a higher pressure that the air passing below, so to equilibrate it tends to search its way down. Side skirts help maintain those two flows of air separated, so that the ground effect is not lost. The side skirts follow suit with the front splitter, consisting on a flat plate which runs parallel to the ground. Table 5.4 (Annex 3) and Fig. 5.4.1 show the main results obtained for two different skirts, with increasing length, compared with the standard AB without skirt, while Fig. 5.4.2 shows the pressure contour for skirts number 2.

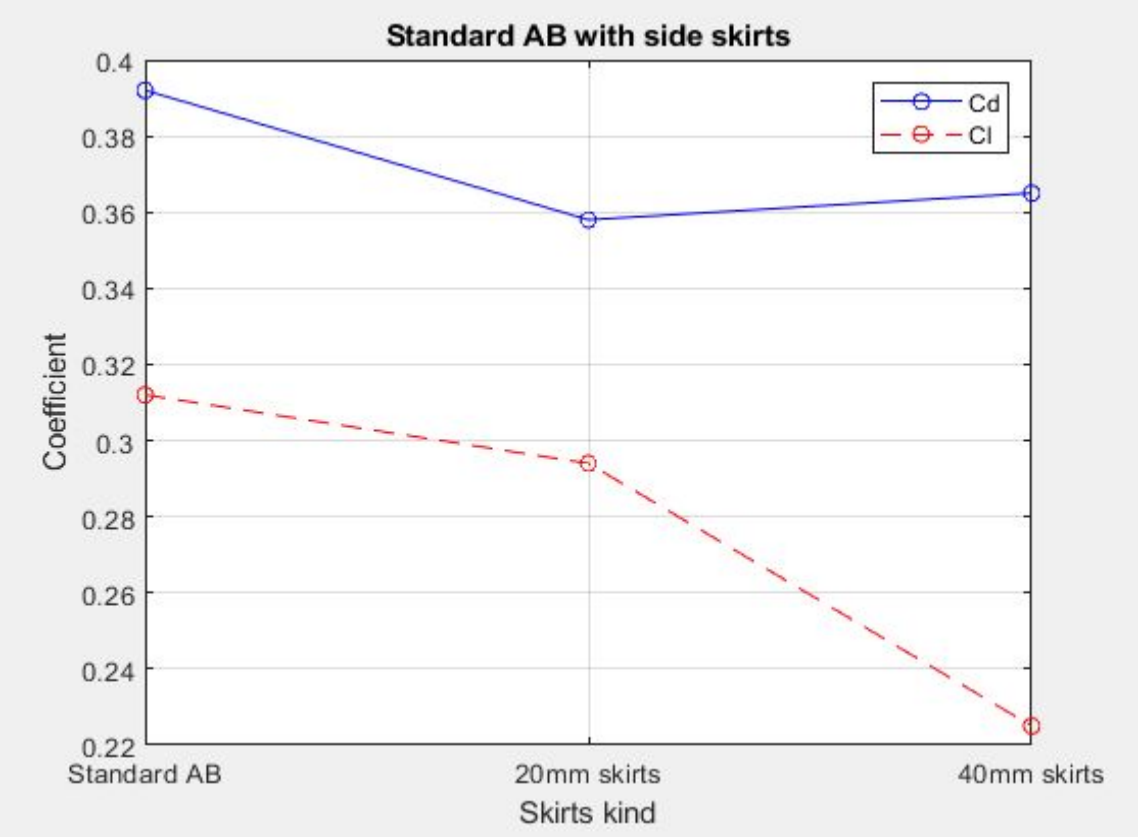

Figure 5.4.1: Force coefficients for standard AB with various side skirts

Side skirts affect both lift and drag in the following manners:

- Lift is reduced proportionally with the size of the skirts, due to the extra planar area provided. When the high-pressure air passing above the car searches its way down to the low-pressure area, it eventually encounters the side skirts in a perpendicular way, and high pressure is built above them, which coupled with the lower pressure found below, gives downforce in return. The effect is similar to that of the splitter.

- Drag decreases due to the fact that side skirts introduce the formation of turbulent vortices at the end of their tips. In blunt bodies, where pressure drag dominates over skin friction drag, a turbulent boundary layer can provide the benefit of a delayed flow separation, and thus a smaller wake and pressure drag. Another explanation could be that side skirts enhance the ground effect by being located relatively close to the ground, where the skirt-tip vortices are affected by the proximity of the ground. The decrease in drag could also be caused by inaccuracy or uncertainty of the simulation, given its relatively small magnitude (about 10% drag decrease).

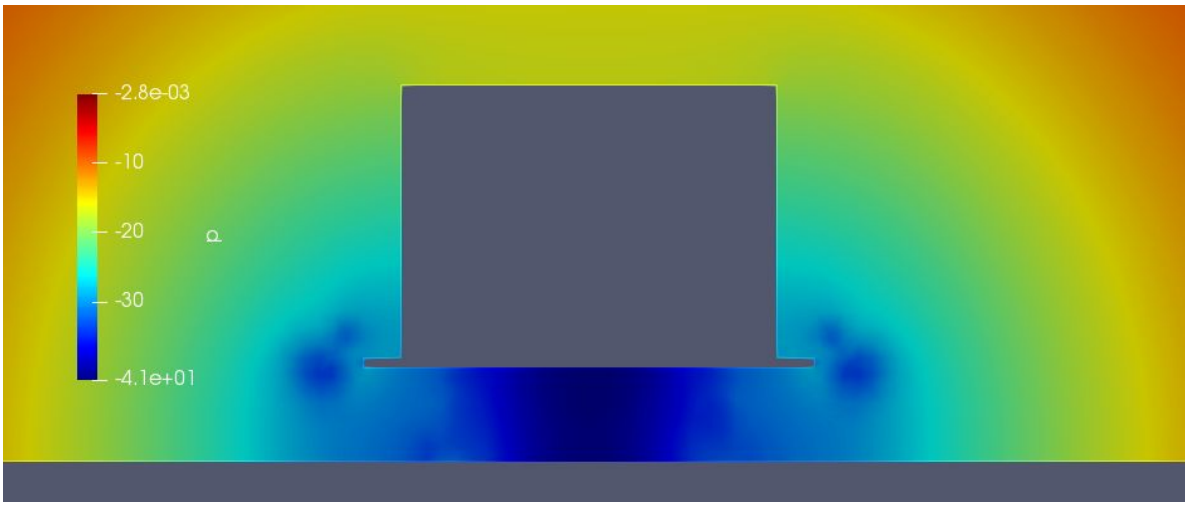

Figure 5.4.2: Pressure over density (m^2/s^2) contour plot for standard AB with 40mm side skirts

5.5. Diffuser

The diffuser's purpose is to cause an adiabatic compression of the air that passes below the car. Said air pressure is usually below the atmospheric pressure, and upon arriving at the rear edge of the car, it is convenient to compress it and try to return its pressure to ambient pressure. If the transition between the small volume found below the car and the big volume behind it happens too abruptly, flow detachment could occur, and therefore undesirable form drag could appear. With the diffuser, a zone of even lower pressure is formed at the edge of the body, which helps with downforce (see Fig. 5.5.1 below). A similar phenomenon can be observed at the car's roof, where the convex shape helps accelerate the air, and therefore reduce its pressure. Note that diffusers have been tested in this work at optimal ride height (100mm) and with side skirts included, since there is a close relationship between them.

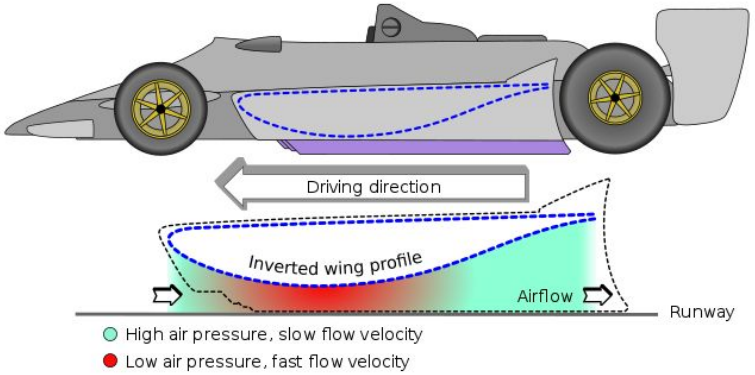

Figure 5.5.1: Diffuser profile of a racing car

Table 5.5 (Annex 4) and figure 5.5.2 show the obtained results for the three different diffuser configurations that have been implemented: at 5, 10 and 15º of ramp angle. Theoretically, a more aggressive ramp angle is able to generate more downforce: the sharper the change in surface angle, the more the flux is accelerated and hence, the lower pressure is achieved. If the pressure is lower below the car with respect to that of above, the pressure difference is bigger and so is the downforce, up to a certain point. Similarly, with wings, a certain angle exists where “stall” starts to take place: in this case, past 10º the increase in downforce is minimal, while the increase in drag starts to be more significant.

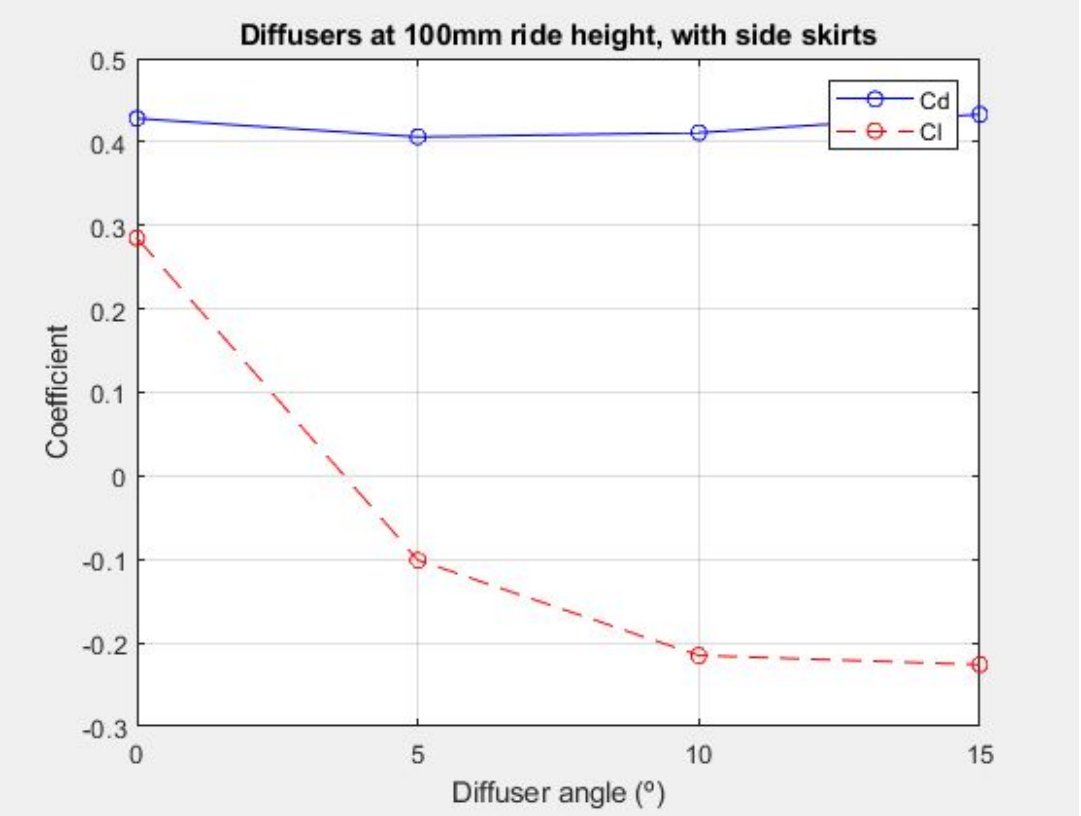

Figure 5.5.2: Force coefficients for standard AB with diverse splitters

From standard AB to 5º diffuser, though, drag is reduced. This can occur due to 2 reasons:

- The rear end area perpendicular to the X axis (that is, the cross-sectional area) is reduced, and since the flow stays attached for 5º ramp angle, the wake is reduced, which means less pressure drag.

- Promoting an early transition of the boundary layer over a blunt body from laminar to turbulent can often reduce the pressure drag, due to a delayed boundary layer detachment thanks to the increased resistance of turbulent

boundary layers to the adverse pressure gradient. This effect can commonly be observed on golf balls: the dimples on their surface introduce turbulence to the flow around it, which is more resistant to detachment, although it implies increased skin friction.

5.6. Rear wing

One of the most common aerodynamic devices, if not the most, found on both race cars and road vehicles are wings. Their purpose is the same of those that can be found on aircraft: generating lift. But while aircraft wings are generally designed to generate positive lift (that is, pointing upwards), car wings are intended to generate negative lift, commonly referred to as downforce.

While downforce should be evenly distributed across the car's body in order to be more advantageous, traffic laws tend to be very restrictive on devices that protrude outside of the car's surface, especially if they are prone to cause damage in case of an accident (e.g. front splitters). Wings are usually located on the back of the vehicle and far from the ground. That is why a lot of car manufacturers use them in road-going vehicles. There are two main types of car wings, although the name wing is commonly used to refer to both of them, or it is sometimes misused:

- Spoilers: spoilers consist in flat plates located at the edge of the trunk, with a certain angle with respect to the flow (see Fig. 5.6.1). While spoilers do not generate lift in the same manner as airfoils do, they can provide downforce to the rear axle by acting as an extended area on which air can stack up and build a high-pressure zone, where pressure is higher than that in the diffuser area, so the outcome is a net positive force pushing the car downwards.

Figure 5.6.1: Example of a rear spoiler

- Wings: Rear wings are airfoil-shaped surfaces placed upside down with respect to typical aircraft wings (see Fig. 5.6.2). That is, contrary to airfoils of aircraft wings, airfoils of car wings have negative camber. The trailing edge is higher than the leading edge, so the air gets deflected upwards, and the resulting force pushes the car to the ground. Wings can be built with one or several “airfoil types”, depending on the amount of downforce wanted, but generally drag also increases as they become bigger and/or more complex.

Figure 5.6.2: Example of a rear wing

Table 5.6 (Annex 5) and Figs. 5.6.3 and 5.6.4 show the main results obtained for three different types of spoilers and rear wings, with increasing AoA, compared with the standard AB without spoiler or rear wing. The behaviour of both spoiler and wing is quite similar: with increasing AoA, the downforce increases. There is, however, a point where flow detachment occurs, leading to stall. For the wing used, NACA 6412, the experimental stall angle is for an AoA around 15 degrees (angle of maximum lift for Re > 500000). Hence, there is no point on increasing AoA further than said angle value, since the downforce obtained is already considerably good.

As for the spoiler, since its name states, it is used to “spoil” the smooth airflow found in the tail of some cars to prevent positive lift. Low angle spoilers are mostly used in drag racing cars as an extension of the trunk that usually runs almost parallel to the trunk’s line. By doing so, the turbulent wake is delayed and appears later, so its size is a bit smaller: this can explain the small decrease in drag for 10º spoiler. As we increase the angle, though, the exposed area starts to increase also, and drag follows suit.

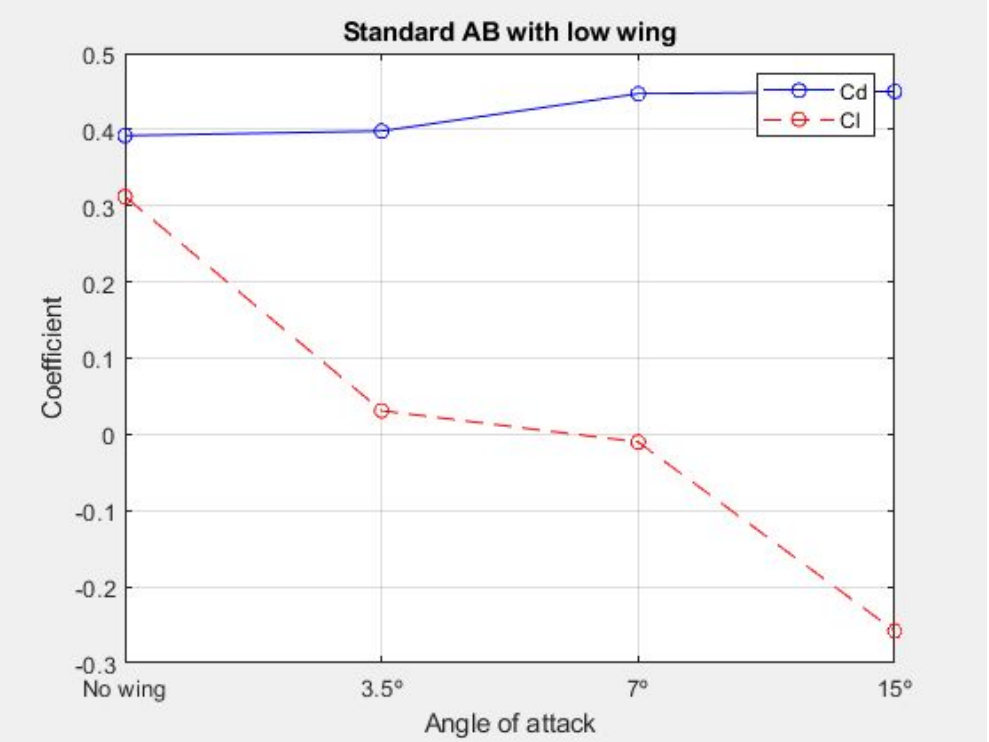

Figure 5.6.3: Force coefficients for standard AB with different wings

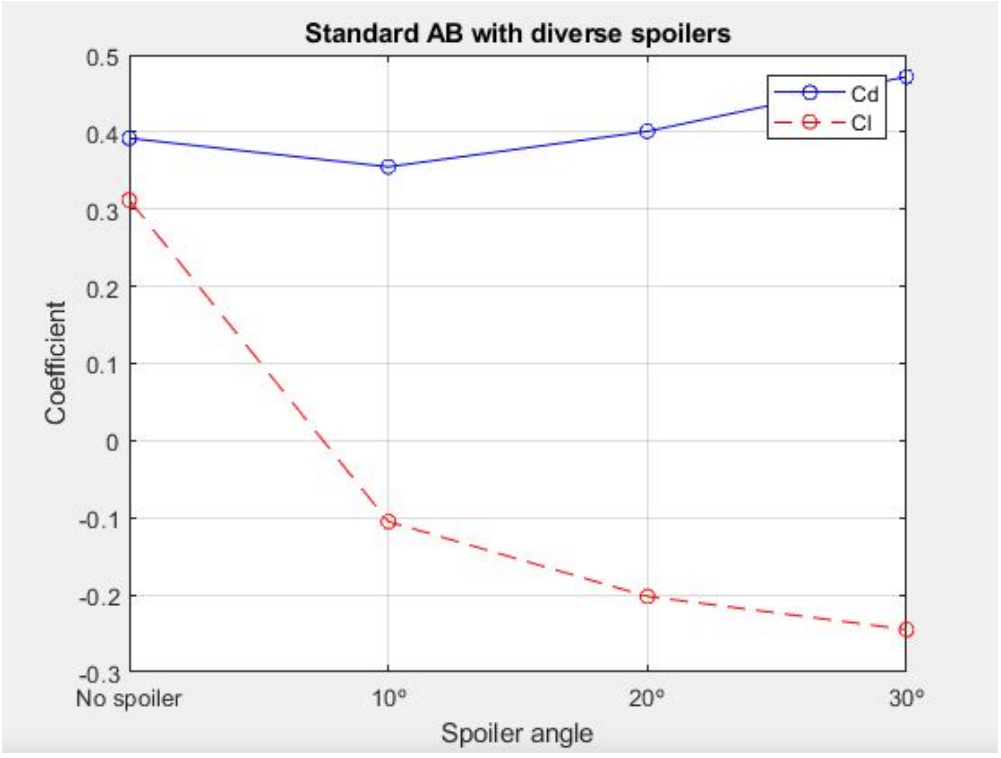

Figure 5.6.4: Force coefficients for standard AB with different spoilers

CHAPTER 6. Influence on the initial model

Once all the components have been analysed separately, we must see how the complete model behaves. For that purpose, the configurations of the components that have proved to generate more downforce when considered individually will be incorporated on the baseline Ahmed Body model, which will be defined as “final AB1”. Those are as follows:

- 100mm ride height
- Single front splitter
- 40 mm side skirts
- 15º diffuser
- Low wing at 15º AoA

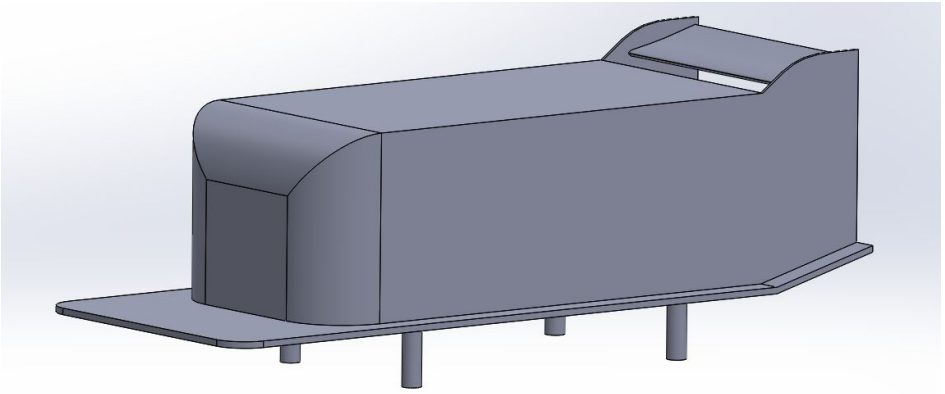

Figure 6.1: Final AB1 model, configuration for maximum downforce of each individual component

Due to the increased geometrical complexity of this model with respect to the initial one, a finer mesh has been used in the region close to the body, with a surface refinement level of 8 with respect to the background mesh and approximately 1.9 million cells This means that the first hexahedral cell of the free stream region, out of the boundary layer, measures now 0.00316 m. Maintaining the same mean value of y^+ = 100 as before, the addLayers parameters had to be modified to adapt the BL growth rate and final layer thickness. Tables 6.1 s and 6.2 show the mesh parameters for this case, and the results obtained from the simulation of final AB1, respectively.

Table 6.1 - Mesh parameters for final AB1 model

First layer [m]	Nº layers	Exp. ratio	Final layer [m]	Overall [m]
1.8E-3	4	1.2	3.11E-3	9.66E-3

Table 6.2 - Forces and force coefficients for final AB1

Variable	Default Ahmed Body	Final Ahmed Body
Lift coefficient	0.312	-0.910
Drag coefficient	0.392	0.537
Efficiency (L/D)	0.795	-1.694
Drag (N)	10.75	15.42
Lift (N)	8.56	-26.07

Force coefficient monitors and residual values show acceptable convergence for the final model (see Figs. 6.2 and 6.3 in annexes 7 and 8). However, note that, in this case, the presence of the appendices introduces more turbulence, especially the wing and side skirts. Residual values do not go as low as they did for the base model (all of them fall below 1%, except U_y, left on 2%).

Another interesting fact is that instead of having downforce for the front axle, we now have positive lift (Cl(f), lift coefficient for the front half of the model), despite having used the 200mm front splitter, which produced negative lift when implemented alone over the initial model. One reason for such behaviour could be the following: the fact that the downforce for the rear axle or rear half of the body (defined as Cl(r)) is much higher than that of Cl(f) could be overcompensating and tilting the body in a clockwise manner. In fact, notice how the moment coefficient (Cm) has increased significantly and is now positive, contrary to what happened in the initial model (see figure 6.2 in Annex 7). This means that, although the overall downforce has increased, it is not evenly distributed between the two halves of the body.

This can be interpreted in the following manner: real life car tires do not behave as classical friction theory would suggest due to tire load sensitivity: the coefficient of friction actually decreases as the vertical load increases [11]. That is why the positioning of the center of gravity and the load distribution are key factors when building a race car. The position of the center of gravity is affected in several ways,

especially when taking a turn. In addition to the standard load distribution of the vehicle, where engine and transmission, generally the heaviest components, will have a greater impact, one should account for the aerodynamic loads too. Adding too much downforce to one of the axles can actually cause loss of traction. The disparity shown in figure 6.2 (annex 7) could be solved in two ways:

- Subtracting one of the components from the rear of the vehicle. Note that both wing and diffuser mainly affect Cl(r), while only the splitter directly affects Cl(f).

- Adding another component to the front of the body: for example, canards. Canards can either be flat or curved plates tilted in a counterclockwise manner from their front tip (located near the front of the vehicle).

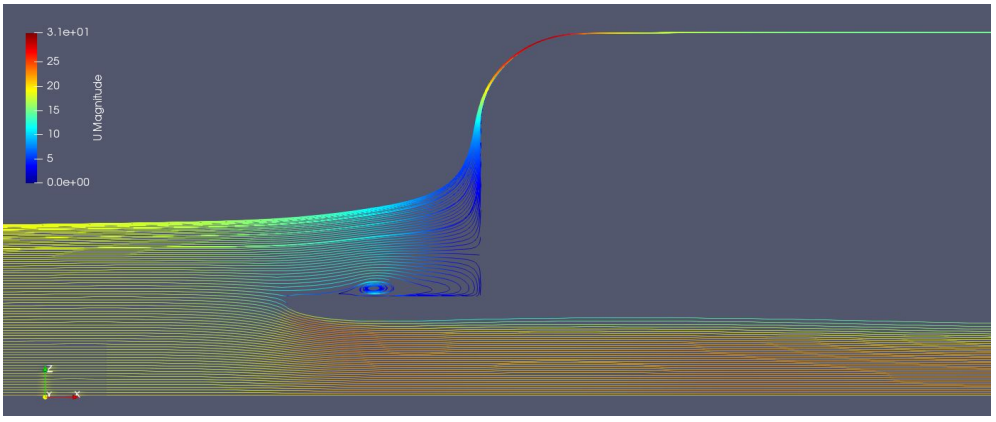

Figure 6.4: Flow velocity streamlines for the front of final AB1 on symmetry plane

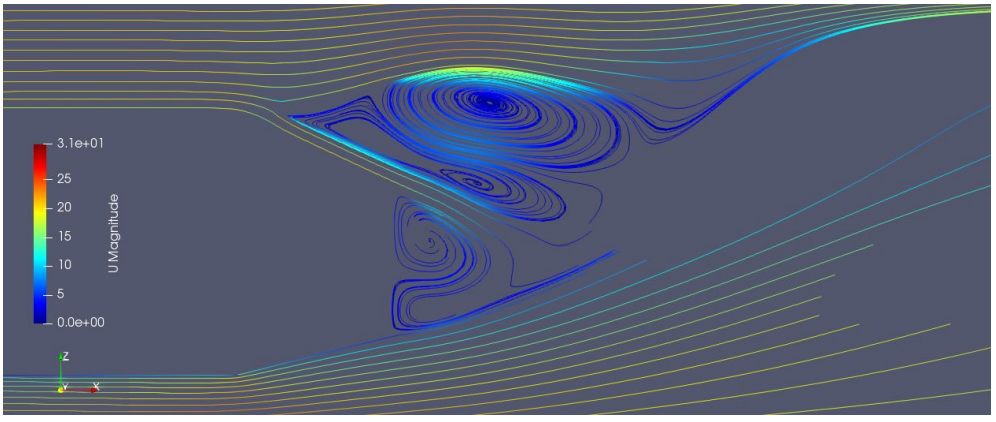

Figure 6.5: Flow velocity streamlines for the back of final AB1 on symmetry plane

The addition of the different components has led to an increase of about 36.98% in drag, as was already expected due to the increase in exposed area (wet surface, where skin friction acts) and the more complex geometry. Also, the presence of the wing increases the intensity of the downwash turbulent wake, which in turn results in higher form drag. On the other hand, while the standard Ahmed Body produced positive lift, the final model is able to generate effective downforce, as the negative lift coefficient demonstrates. Its magnitude is also important: the downforce force generated is almost three times the initial positive force in absolute terms.

One common scenario that can be observed for most lift devices such as wings or splitters is that one can achieve a good amount of lift while only increasing the drag slightly. This means that most of the times, the increase obtained in lift by using said devices means a bigger advantage, comparatively, than the drag decrease obtained by not using them. In fact, the decision of implementing a more or less aggressive aerodynamic setup depends on the specific track, among other factors: for a slower track with more turns, like Monaco circuit, more downforce could be advantageous for taking the turns at the highest possible speed. On the other hand, in a circuit like Nürburgring, which has fewer, wider turns and longer straight legs, having less drag would be preferable for reaching higher top speeds in the straight legs. Note the gradual pressure reduction under the body and the correspondent flow acceleration, which peaks in the diffuser zone, as depicted in Fig. 6.6.

Table 6.3 - Percentage change in force coefficients over final AB1

Variable	**Change (%)**
Drag	+36.98
Downforce (front)	-9100
Downforce (rear)	+351.61
Downforce (total)	+291.66
Pitching momentum	+418.3

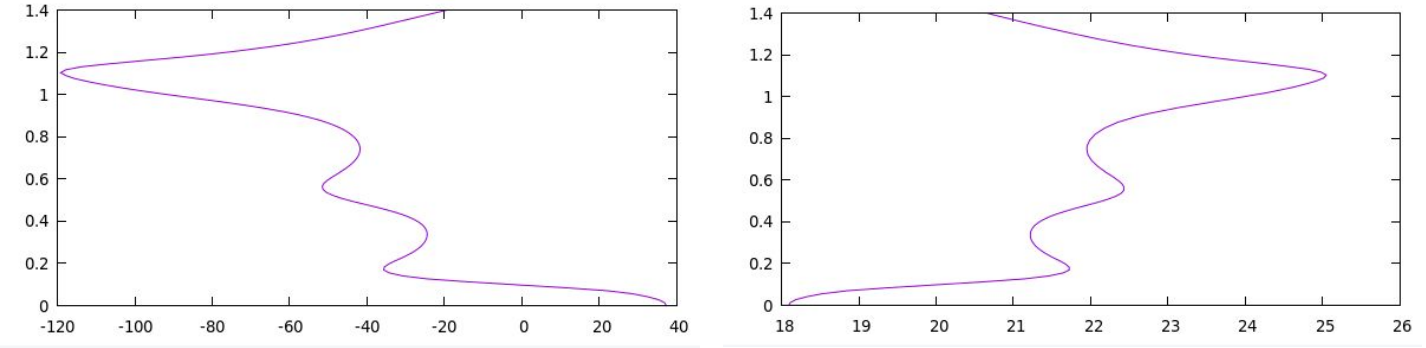

Figure 6.6: Pressure over density (left, m^2/s^2) and flow velocity (right, m/s) vs. length over X axis, 0.05 m height

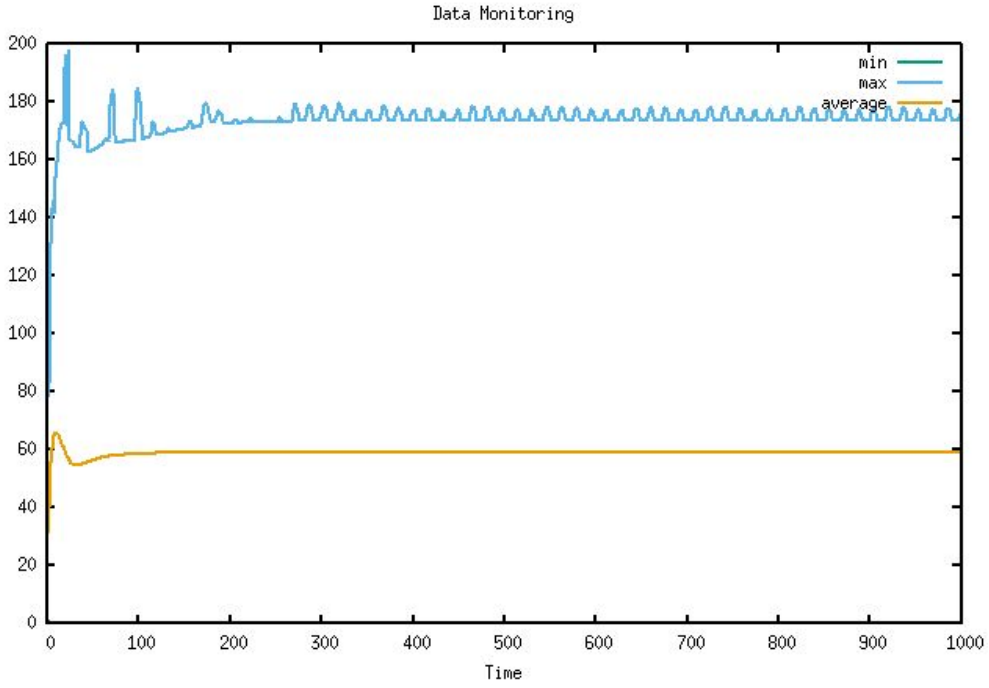

Figure 6.7: y^+ vs. time

6.1. Geometry with additional components

Since the downforce observed in the final model has increased in a heterogeneous way, a set of canards has been implemented in order to balance the downforce distribution between front and rear axles. In this case, the purpose is to provide more downforce to the front section of the body.

Two types of canards have been tested: flat plate and curved plate. Both have their chords with the same length as that of NACA 6412 airfoil used for the wing, and are offset to 20 degrees.

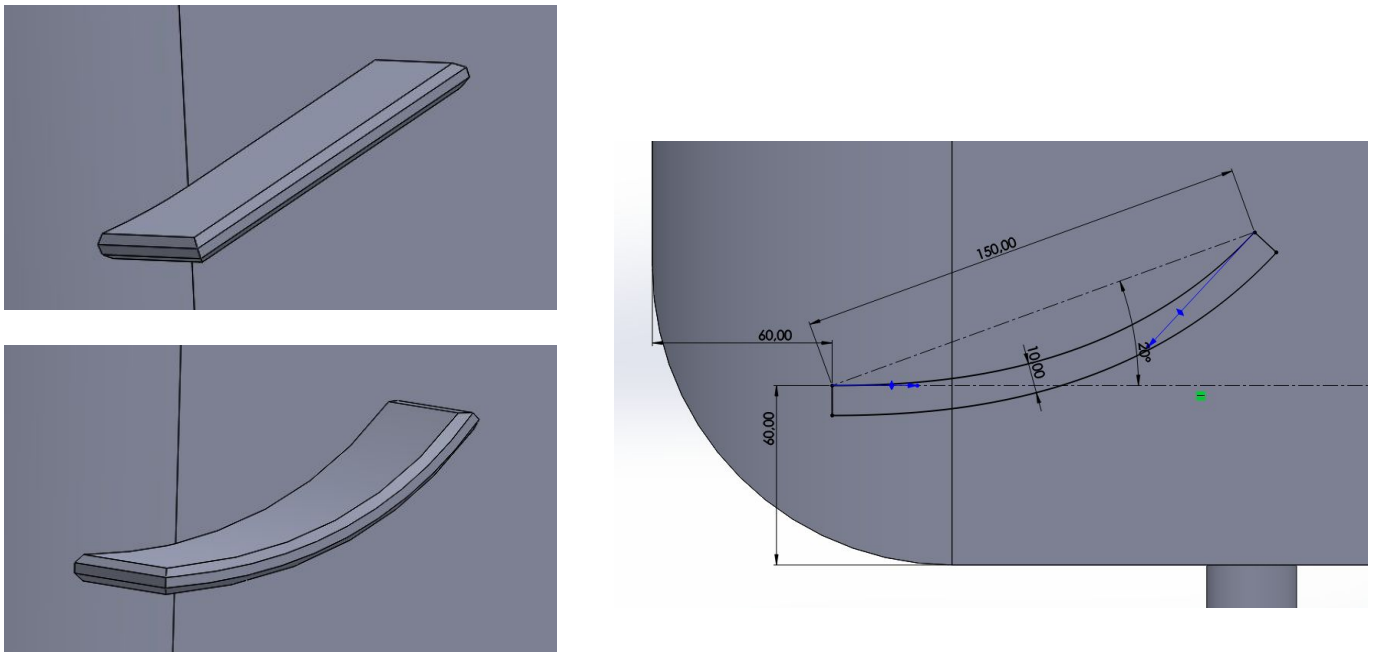

Figure 6.1.1: Sketch (right) and final build of the canards (left)

Table 6.1.1 - Force coefficients for standard AB with different canards

Model	**Lift Coefficient**	**Drag Coefficient**	**Efficiency (L/D)**
Standard AB	0.312	0.392	0.795
Flat canards	0.173	0.335	0.516
Curved canards	0.133	0.342	0.388

Even though the chord angles are the same in both models, curved canards have proved to offer more downforce, much like airfoils usually produce more lift than flat plates.

Notice also the drag reduction due to the aforementioned vortex induction on the tip of the canards: they act much like side splitters for that matter. Curved canards are implemented next to the final model.

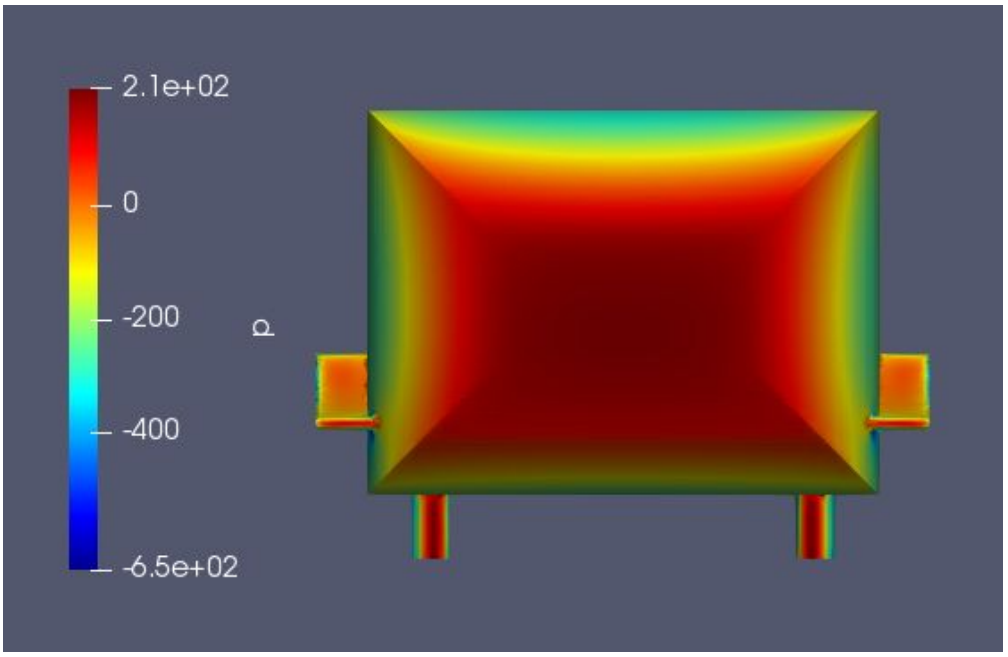

Figure 6.1.2: Surface plot of pressure over density contour on standard AB with curved canards (units in m^2/s^2)

6.2. Final model over Ahmed Body - second version

The last model, implementing curved canards, has proven to provide the greatest overall downforce, while also balancing a bit the relationship between Cl(f) and Cl(r), as Table 6.2.1 below demonstrates.

Table 6.2.1 - Force coefficients obtained for final AB1 with canards

Model version	**Lift Coefficient**	**Drag Coefficient**	**Efficiency (L/D)**
Standard AB	0.312	0.392	0.795
Final AB1 v.1 (no canards)	-0.910	0.537	-1.694
Final AB1 v.2 (canards)	-0.957	0.574	-1.519

Table 6.2.2: Lift coefficient at front and rear, and pitching moment coefficient obtained for final AB1 with canards

Model version	**Cl (front)**	**Cl (rear)**	**Cm (torque)**
Standard AB	0.002	0.310	-0.156
Final AB1 v.1 (no canards)	0.415	-1.325	0.87
Final AB1 v.2 (canards)	0.215	-1.172	0.697

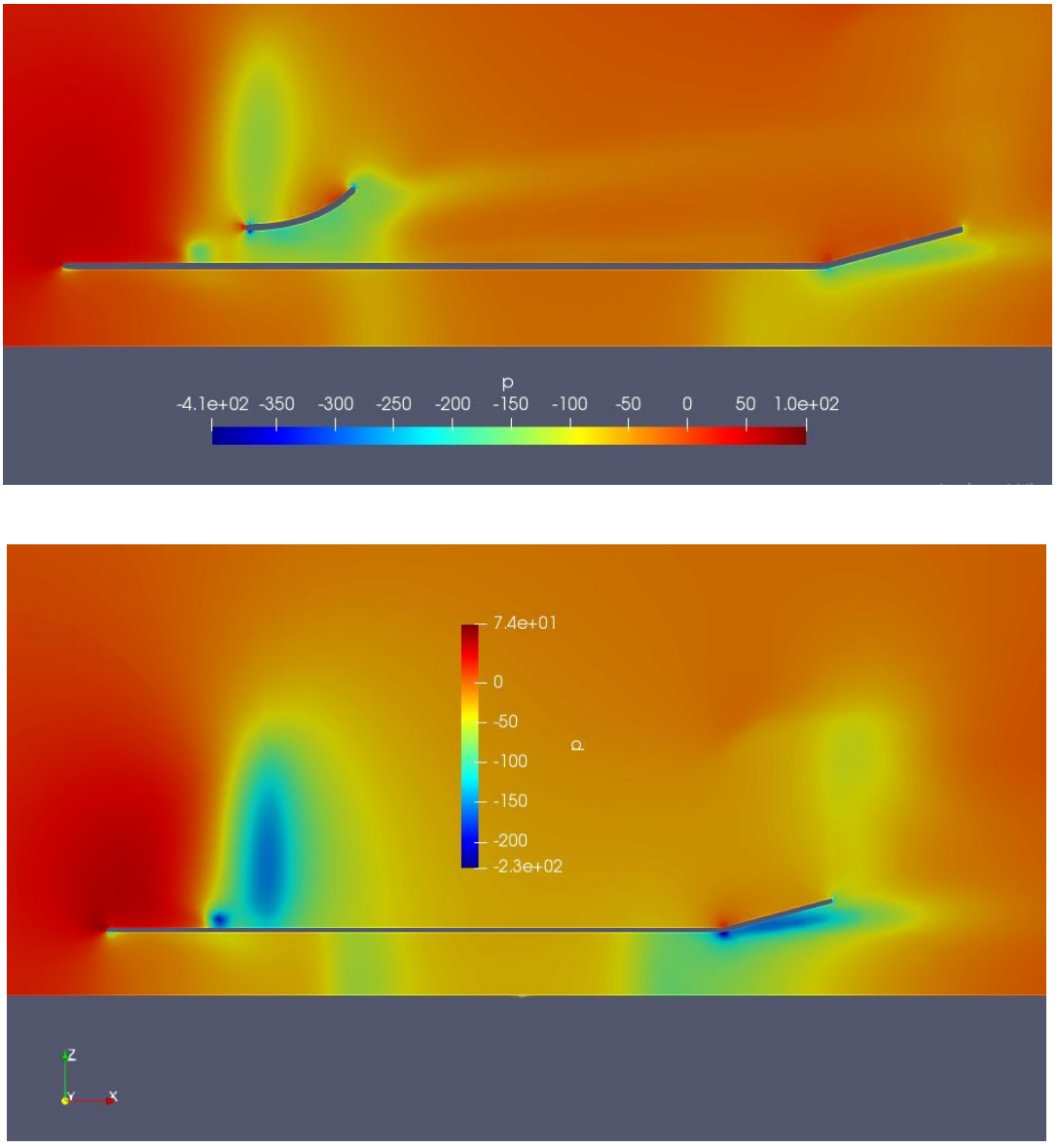

Figure 6.2: Pressure over density (m^2/s^2) plane cuts on versions v.2 (above) and v.1 (below)

6.3. Comparison of different configurations for maximum downforce assessment

In order to verify that the maximum downforce for final AB model is achieved by using all of the components that demonstrated the highest contribution to downforce when studied individually, two more final AB configurations have been studied. Considering the high number of possible combinations between all the developed components, this section aims at testing different configurations than the one initially considered to be the optimal, and see how the model behaves.

Final AB2 consists on implementing all the second most effective components at downforce production over standard AB at 25 mm ride height, to see if it is possible to maintain an acceptable value of downforce while trying to decrease drag as much as possible. The results obtained previously show that, generally, our second-best component configurations still provide good downforce when compared with the ones that provide the highest downforce, while producing slightly less drag, when studied individually. Note that “best” is assumed here in terms of highest downforce contribution.

Final AB3 consists on implementing a random mix of best and second-best component configurations over standard AB at 50 mm ride height, to assess how a change in ride height could affect the behaviour of the fully built model, not just the standard version. As stated before, the number of possible combinations is quite high, so final AB3 will serve as a random sample from that wide pool of options. Further investigation in this regard has been compromised by lack of time.

6.3.1. Final AB2

The results obtained for final AB2 show a decrease in downforce with respect to final AB1 (-0.615 for final AB2, -0.957 for final AB1; that means a decrease of 55% in downforce). This demonstrates that the individual behavior of the components translates to a similar behavior of the configurations, where the single components are united: less individual downforce means less combined downforce in this case. In regards of drag, a decrease of 14.62% can be observed (0.467 for final AB2, 0.547 for final AB1). The behavior of the appendices with respect to drag is similar to that of downforce in this model: less individual drag for all of the components demonstrates a lower combined drag for the final model. Efficiency for this model is -1.316.

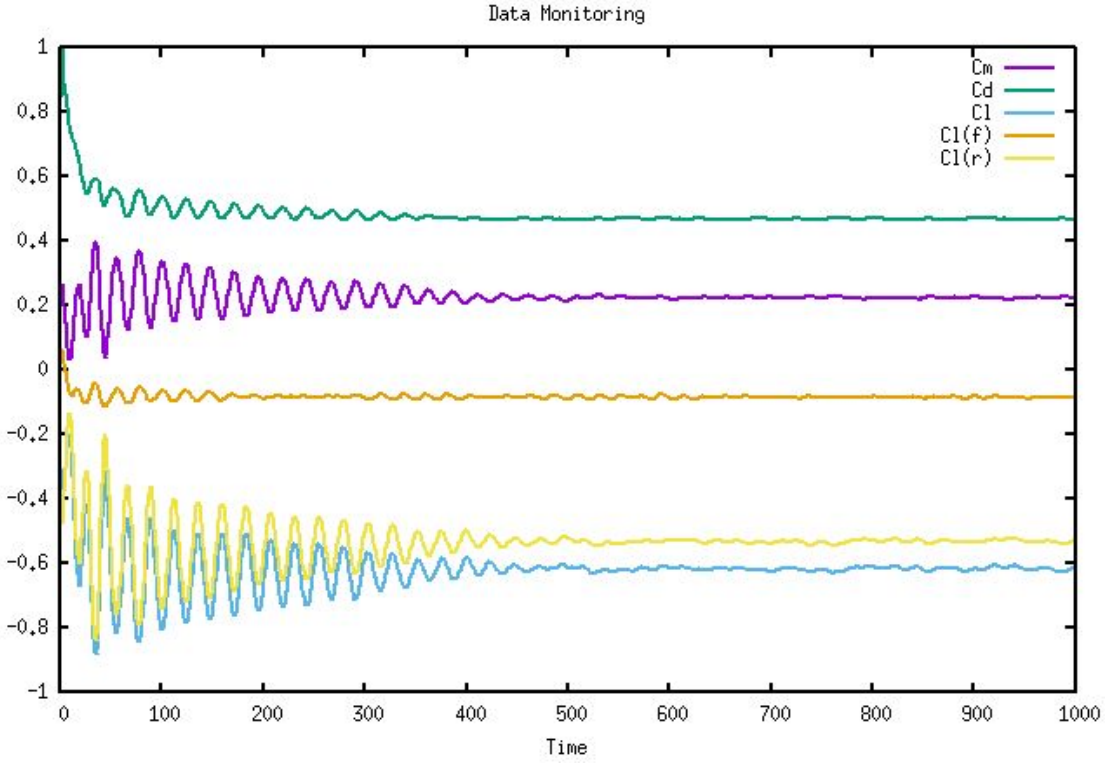

Figure 6.3.1: Force coefficients for final AB2

6.3.2. Final AB3

As stated before, final AB3 incorporates a random mix of components, so its behaviour is a bit more difficult to predict. The results obtained for final AB3 show that the downforce has been maintained at a value close to that of final AB1 (-0.957 for final AB1, -0.852 for final AB3; that is, downforce is 11% smaller), while drag has decreased 18% (0.547 for final AB1, 0.458 for final AB3). The higher decrease in drag when compared with final AB2 could be explained by the lower ride height used in final AB3 (50 mm), which supposes less drag when considered individually (0.392 for 50 mm, 0.428 for 100 mm). Regarding downforce, the fact that final AB3 incorporates some of the configurations producing highest downforce could explain the increase (38.25%) with respect to final AB2 (-0.615 for final AB2, -0.852 for final AB3). Efficiency is thus slightly better (8% higher) for final AB3 (-1.893) when compared with final AB1 (-1.749), although final AB1 remains as the configuration which demonstrates the highest total downforce.

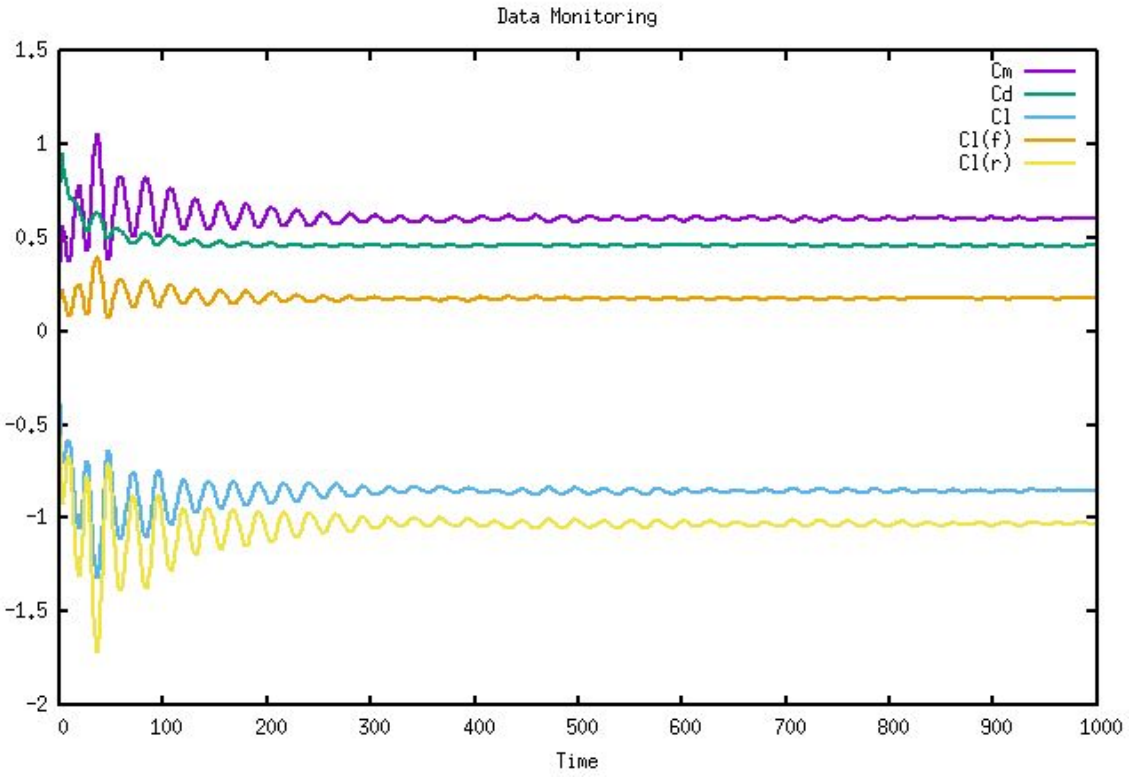

Figure 6.3.2: Force coefficients for final AB3

CHAPTER 7. Developed geometry over 2017 Audi R8 V10

As a final section to this project, the different add-ons previously developed and tested over standard Ahmed Body which demonstrated the highest contribution to downforce generation are now implemented over a simplified model of a 2017 Audi R8 V10. The original intention was to work directly with this model, but no reliable aerodynamic data was found about it, nor published CFD studies over this kind of geometry. Moreover, the Ahmed Body offered a reference platform on which the effects of the tested add-ons would likely be more distinguishable in absence of the geometric complexities and specificities of the particular 2017 Audi R8 V10, and it is arguable that the behaviours observed on the Ahmed Body would probably be more easily generalized to other geometries compared to the hypothetical trends observed for the 2017 Audi R8 V10.

Both the Ahmed Body and the simplified R8 model are bluff bodies. But although the latter got rid of body details, rotating wheels and internal components, their shapes and sizes are substantially different, with the R8 having a closer shape to a road-going car. Based on the premise that the latter would make for a more realistic approach to an actual car behaviour, the appendices have been resized and adapted to this new geometry. Two tests have been carried out: one over the standard R8 model, and the other on the final R8 model. Both are compared below.

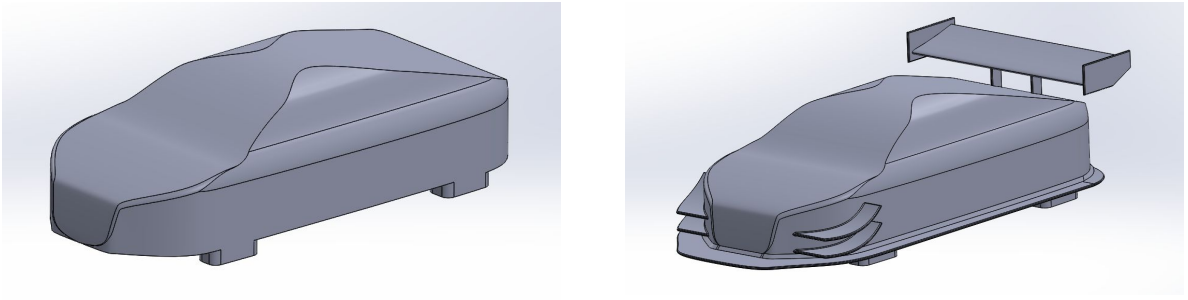

Figure 7.1: Standard R8 model (left) and final R8 model (right)

- Length: 4426 mm
- Width: 1925 mm
- Height: 1260 mm
- Canards and wing chords: 273 mm
- Wing height: 470 mm
- Diffuser length: 340 mm

- Splitter length: 380 mm
- Side skirts length: 73 mm

Notice that the ride height has been left at its default value: 560 mm. The assumption here is that the engineers at Audi know exactly what is the optimal ride height for a car like this, and scaling the ride height from Ahmed Body to this model left it at an unusually high distance from the ground, considering it is a sports car.

Given that the reference length has now changed from 1.044 to 4.426 meters, the Reynolds number is also different, and so are the initial conditions for turbulence, which had to be recalculated. y^+ value also varies with reference length. The new calculated values for this model are shown in tables 7.1 and 7.2.

Table 7.1 - Reynolds number and initial turbulence parameters for R8 models

Reynolds number	**I (turb. intensity)**	**k (turb. kinetic energy**	**w (specific turb. dissipiation rate)**
6.0E6	0.02274	0.3103	4.501

Table 7.2 - Layer addition parameters for R8 models

First layer [m]	**Nº layers**	**Exp. ratio**	**Final layer [m]**	**Overall [m]**
1.8×10^{-3}	5	1.5	9.1×10^{-3}	0.0237

The methodology for the simulation has been kept the same, except for the wind tunnel: it has been enlarged by 10 m upwind and 15 m downwind, to comply with the rules stated in section 3.3.1; the tunnel now measures 45 x 8 x 8 m. Aside of that, the solver, turbulence model and number of iterations have remained equal. Tables 7.3 and 7.4 show the comparison of the results for both the standard R8 and the final R8.

The effects observed are similar to those found on the final AB models. Downforce has increased significantly, while the increase in drag has been greater than the one seen on the final AB models. That could be due to several factors, namely:

- Uncertainties of the simulation.
- The fact that the model used is extremely simplified when compared to the real Audi R8 (no details over the body, no rotating wheels, a flat undertray, no internal flow of air).
- Given the difference (51.35%) in drag coefficients between standard AB (0.392) and standard R8 (0.259), when combined with the fact that the implemented components over final R8 model are comparatively bigger in area than those in final AB models, could mean that the aerodynamic appendices have a more prominent effect on the less draggy vehicle (the final R8).

In this case, though, downforce is achieved for both front and rear axles, so it is more homogeneously distributed over the whole model. As a result, the pitching moment coefficient has been kept at a lower value when compared with final the AB cases.

Table 7.3 - Force coefficient comparison for standard R8 and final R8 models

Model	**Lift Coefficient**	**Drag Coefficient**	**Efficiency (L/D)**
Standard R8	0.297	0.259	1.146
Final R8	-0.689	0.680	-1.022

Table 7.4 - Lift coefficient for both front and back, and pitching moment coefficient for standard R8 and final R8 models

Model	**Cl front**	**Cl rear**	**Cm**
Standard R8	- 0.132	0.429	- 0.280
Final R8	- 0.131	- 0.558	0.225

7.1. Influence of the developed components over final R8

The final configuration of the components implemented over the final R8 model has proven to be effective in the task of generating downforce, as the results in tables 7.3 and 7.4 showcase. But increased downforce also means increased drag, and those two factors have an influence on the car's performance.

7.1.1. Study on turn velocity

Downforce has a similar effect as increasing the load on the vehicle: the friction between the tires and the ground increases, and the traction is improved. The equations shown below assess the influence of downforce in a turn situation:

- X axis: (eq. 7.1.1)

$$F_R = m \cdot a_n = m \cdot \frac{v^2}{R}$$

- Y axis: (eq. 7.1.2)

$$N = W + L$$

Considering that: (eqs. 7.1.3 and 7.1.4, successively)

$$F_R = \mu \cdot N = \mu \cdot (W + L)$$

$$W = m \cdot g$$

A relationship between velocity and downforce can be inferred: (eq. 7.1.5)

$$\mu \cdot (m \cdot g + L) = m \cdot \frac{v^2}{R}$$

For a fixed μ (friction coefficient with the ground), a fixed turn radius R and a given mass m, an increase in downforce would suppose a higher speed for the

vehicle to be able to take the turn. For a comparison of the limit speed at a turn between standard R8 and final R8, a case can be set up. Let us assume a friction coefficient of 0.8 [18], a turn radius of 50 m, a gravitational acceleration of 9.81 m/s^2 and a mass of 1600 kg, the standard dry weight for the 2017 Audi R8 V10 plus a 70 kg rider and 5 kg of fuel. Rearranging for velocity and substituting the aforementioned variables, equation (7.1.5) would then reduce to the following: (eq. 7.1.6)

$$v = \sqrt{2.5 \times 10^{-2} \cdot (15696 + L)}$$

Calculating the lift coefficient generated by both standard R8 and final R8 as (eq. 7.1.7)

$$L = \frac{1}{2} \cdot \rho \cdot S \cdot v^2 \cdot C_L$$

Using $v = 20\ m/s^2$, $\rho = 1.225\ kg/m^3$, $S = 2.01\ m^2$ and the obtained C_L for each model, we obtain 146.25 N of positive lift for the standard R8, and 339.3 N of negative lift for the final R8. Substituting both forces on equation 7.1.6 we obtain the velocities shown in table 7.1.1.

Table 7.1.1 - theoretical maximum turn velocities for R8 models

Model	**Theoretical maximum velocity**
Standard R8	19.71 m/s
Final R8	20.02 m/s

The final R8 model sees its turn velocity increased by 1.57%. The difference may not seem like much, but let us consider a lap around a track which has 10 turns like the one described above, assuming the turns to be half a circumference and assuming also a constant velocity all around the track: said track would measure 1570 meters in length. The driver in the final R8 would be scoring lap times of 78.42 seconds, compared with the 79.69 seconds of the one driving the final R8, so the difference would be of 1.27 seconds per lap.

7.1.2. Study on consumption

The other side of the coin is the increase in drag that the increased downforce entails. In order to reflect said drag increase in a real life situation, the theoretical power consumption of both standard R8 and final R8 is compared in a constant velocity, straight and level driving situation. If we consider $dV/dt = 0$, the forces acting over the car would be:

- X axis: (eq. 7.1.8)

$$F_m = m \cdot a = F_R + D$$

- Y axis: (eq. 7.1.9)

$$N = W + L$$

Considering again equations 7.1.3 and 7.1.4 and rearranging for F_m, we obtain equation (7.1.10):

$$F_m = D + \mu \cdot (m \cdot g + L)$$

Assuming the same μ, m and g as before, and calculating the drag forces for standard R8 (127.50 N) and final R8 (334 N), then substituting those on equation (7.1.10), the obtained driving force (F_m) for each model is contained in table 7.1.2 below.

Table 7.1.2 - Theoretical driving forces needed for each R8 model to maintain a 20 m/s cruise speed

Model	**Driving force (F_m)**
Standard R8	12567.30 N
Final R8	13162.24 N

The increase in driving force that the final R8 should produce, with respect to that of the standard R8, to maintain a steady velocity is of 4.73%. Thus, more power would be needed, and consumption would increase in a linear way.

The last two sections help to give a rough idea of the advantages and drawbacks of implementing aerodynamic devices over a car. In essence:

- The aerodynamic kit provides effective downforce, which helps with traction and can improve lap times, which is the ultimate goal in racing. On top of that, most of the implemented devices can be fabricated in sheet metal, if one wants to cut the costs, or in lighter and stronger materials, like CFRP (Carbon Fiber Reinforced Polymers) if the budget is larger. In any case, a well developed aerodynamic package can provide significant benefits for a fraction of the cost of upgrading the power plant of a car, for example.

- When comparing the percentage increase in turn velocity with the increase in driving force, and thus consumption, one can state that performance comes at the expense of economical investment. For example, a car cruising at 80 km/h may require only 10 hp (horsepower) or 7.5 kW of power to overcome aerodynamic drag, but that same car at 160 km/h requires 80 hp (60 kW) [19]. That is because drag increases as the square of velocity; on the race track, the increased downforce that aerodynamic components deliver at high-speed turns may suppose an advantage despite the increased consumption, but that is definitely not the case on road legal cars, where said devices are most of the times forbidden if they do not come installed from the factory.

CONCLUSIONS

The objective of the present project was to design, implement and test a variety of external aerodynamic components over a bluff body to assess their behaviour and the effects that they could have on the forces experienced by the body, with the ultimate goal of achieving the highest possible negative lift. A first simulation has been performed over standard Ahmed Body, and the obtained results have been compared with published data to ensure the validity of the methodology used.

Next, the process of designing and testing the aerodynamic components individually has allowed to compare how each of the mentioned acts over the standard AB model. Different configurations for each of the components have been simulated, namely: 3 wings, 3 spoilers, 2 canards, 2 side skirts, 3 diffusers, 2 front splitters and 3 ride heights have been tested. Three final models have been developed over standard AB, and their results have been compared.

Final AB1, which implemented all of the component configurations that demonstrated the highest contribution to downforce when studied individually, showed the highest total downforce of the three final AB models tested. Final AB2, which implemented all of the configurations producing second highest downforce when studied individually, with a ride height of 100 mm, showed a decrease in downforce of 55% over final AB1, but also a decrease in drag of 14.62%. Final AB3, which implemented a random mix of configurations producing highest and second highest downforce over a ride height of 50 mm, showed a decrease in downforce of 11% with respect to final AB1, but also a decrease in drag of 18%.

From the obtained results over the various AB models, a certain tendency is observed: a geometry implementing all of the components in their individual maximum downforce configuration also produced the overall maximum downforce (final AB1). A similar event occured with drag in final AB2. With final AB3 being conformed by a random mix of best and second best downforce producing items, the behaviour observed is a mixture between those of final AB1 and final AB2.

Finally, a simplified model of a 2017 Audi R8 V10 has been developed and tested under the same simulation assumptions as the final AB models. The configuration of appendices used in the final AB1 has been resized and implemented over the R8 model, to assess the behaviour of said components over a more realistic car geometry. The results obtained show a similar behaviour to that observed in final AB models in terms of downforce production (332% increase over standard R8), while in terms of drag, the observed increase has been comparatively higher

(163% increase over standard R8). A study on the influence of the installed components has been conducted regarding turn velocity and consumption. Final R8 has shown an increased turn velocity of 1.57% over that of standard R8, but also an increase in consumption of 4.73%.

REFERENCES

[1] S.R. Ahmed, G. Ramm, *Some Salient Features of the Time-Averaged Ground Vehicle Wake*, SAE-Paper 840300 (1984).

[2] Petteri, T., *Experimental study of the flow around the Ahmed Body*, Final Degree Thesis, Universidad de Granada - Universidad de Málaga (2013)

[3] 2017 Audi R8 V10 5.2 TFSI Blueprints, extracted from: http://www.audi-eg.com/content/dam/ngw/eg/Models/R8/etd_R8_Coupe_5_2_FSI_quattro_S_tronic_449_kW_0515.pdf (2015)

[4] Greenshields, C., "OpenFOAM user guide", extracted from: https://cfd.direct/openfoam/user-guide/ (2017)

[5] Barlow, J.B., Rae, W.H., Pope, A., *Low-speed Wind Tunnel Testing,* 3rd ed., New York, USA: Wiley & Sons, p. 713 (1999)

[6] Ferziger, J.H., Peric, M., *Computational Methods for Fluid Dynamics*, 3rd ed., Berlin, Germany: Springer-Verlag (2002)

[7] Jousef, M., "What is y^+ (yplus)?", extracted from: https://www.simscale.com/forum/t/what-is-y-yplus/82394 (2018)

[8] "Near wall treatment for K-Omega SST turbulence model", extracted from : https://www.cfd-online.com/Forums/openfoam-solving/86855-near-wall-treatment-k-omega-sst.html (2011)

[9] Jousef, M., "Y+ (yplus) - Generate wall spacing for CFD": https://www.simscale.com/forum/t/y-yplus-generate-wall-spacing-for-cfd/82451

[10] Sabán, A., *Análisis del flujo de aire a través de un difusor de automóvil,* Final Degree Thesis, EETAC (2018)

[11] "Tire load sensitivity", extracted from: https://en.wikipedia.org/wiki/Tire_load_sensitivity (2018)

[12] Bakker, A., "Lecture 7 - Meshing", extracted from: http://www.bakker.org/dartmouth06/engs150/07-mesh.pdf (2002)

[13] “NACA 6412 experimental data”, extracted from: http://www.airfoildb.com/airfoils/335

[14] Anderson, J.D., *Fundamentals of Aerodynamics*, 3rd ed., New York, USA: McGraw Hill (2001)

[15] Castaldi, G., “Laminar vs. turbulent flow separation”, extracted from: https://physics.stackexchange.com/questions/197720/laminar-vs-turbulent-flow-separataion (2015)

[16] Lucas, P. W., “Splitter or air dam - Which design is best?”, extracted from: https://hanchagroup.wordpress.com/2013/01/29/splitter-or-air-dam-which-design-is-best/ (2013)

[17] “SIMPLE algorithm”, extracted from: https://en.wikipedia.org/wiki/SIMPLE_algorithm (2018)

[18] “Gestión técnica del tráfico, Dirección General de Tránsito”, extracted from: http://www.dgt.es/Galerias/la-dgt/empleo-publico/oposiciones/doc/2013/TEMA_5_GESTION_TECNICA_TRAFICO.doc

[19] “Drag (physics)”, extracted from: https://en.wikipedia.org/wiki/Drag_(physics)

ANNEXES

Annex 1. *Table 5.2 - Force coefficients and efficiency for standard AB at various ride heights*

Model	Lift Coefficient	Drag Coefficient	Efficiency (L / D)
Ride height 1 (12.5mm)	0.601	0.320	1.875
Ride height 2 (25mm)	0.398	0.337	1.18
Standard AB (50mm)	0.312	0.392	0.795
Ride height 3 (100mm)	0.285	0.428	0.6658

Annex 2. *Table 5.3 - Force coefficients and efficiency for standard AB with various splitters*

Model	Lift Coefficient	Drag Coefficient	Efficiency (L / D)
Standard AB	0.312	0.392	0.795
Splitter 1 (50mm)	0.135	0.385	0.350
Splitter 2 (100mm)	0.121	0.429	0.282
Splitter 3 (200mm)	0.110	0.422	0.260

Annex 3. *Table 5.4 - Force coefficients and efficiencies for standard AB with various skirts*

Model	Lift Coefficient	Drag Coefficient	Efficiency (L / D)
Standard AB	0.312	0.392	0.795
Skirts 1 (20mm)	0.294	0.358	0.821
Skirts 2 (40mm)	0.225	0.365	0.616

Annex 4. *Table 5.5 - Force coefficients for standard AB with diverse splitters*

Model	Lift Coefficient	Drag Coefficient	Efficiency (L / D)
Standard AB	0.285	0.428	0.665
Diffuser 1 (5º)	-0.101	0.406	-0.248
Diffuser 2 (10º)	-0.215	0.411	-0.523
Diffuser 3 (15º)	-0.226	0.433	-0.522

Annex 5. *Table 5.6 - Force coefficients for standard AB with different wings and spoilers*

Model	Lift Coefficient	Drag Coefficient	Efficiency (L / D)
Standard AB	0.312	0.392	0.795
Spoiler 1 (10º)	-0.105	0.355	-0.295
Wing 1 (3.5º)	0.031	0.398	0.077
Spoiler 2 (20º)	-0.202	0.401	-0.503
Wing 2 (7º)	-0.01	0.447	-0.022
Spoiler 3 (30º)	-0.245	0.472	-0.519
Wing 3 (15º)	-0.258	0.450	-0.573

Annex 6. *Figure 5.3.4: Force coefficients for standard AB with splitter 3 (200 mm)*

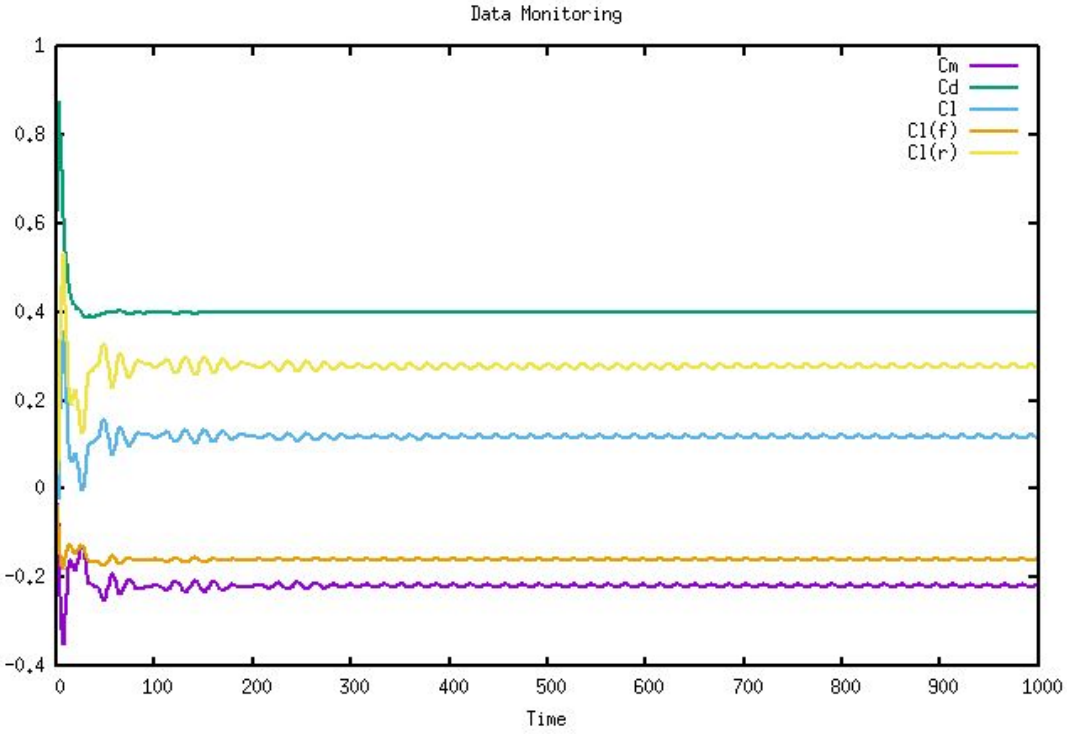

Annex 7. *Figure 6.2: Force coefficients for final AB1*

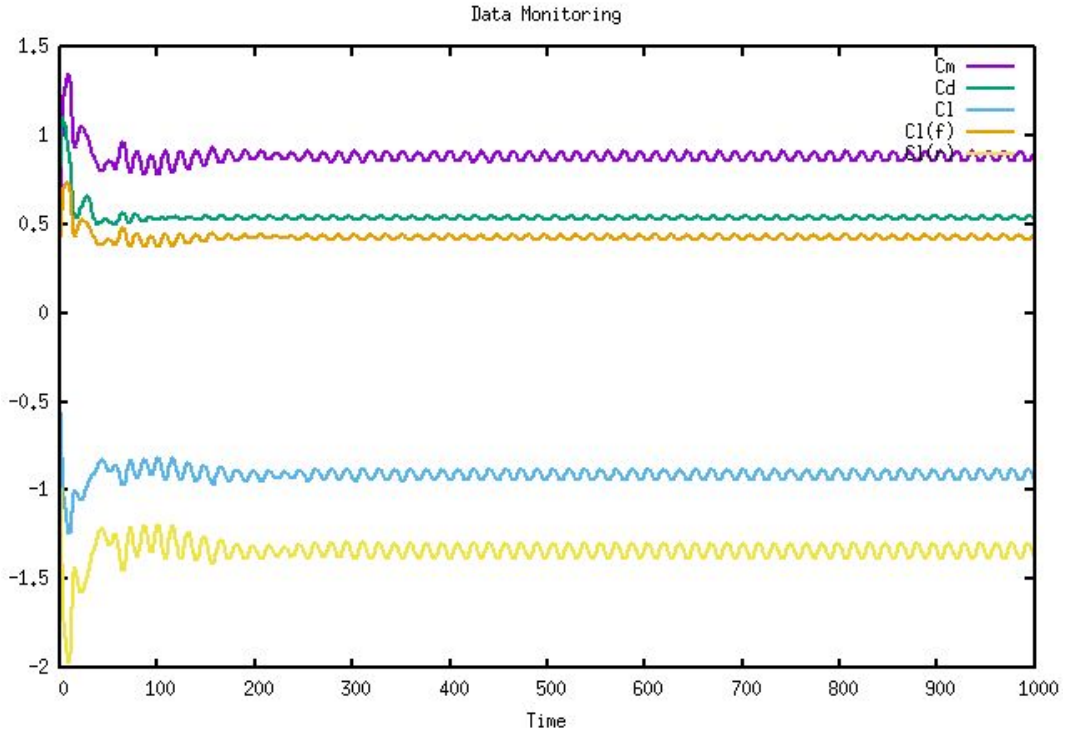

Annex 8. *Figure 6.3: Residuals for final AB1*